THE PENNSYLVANIA STATE UNIVERSITY
SCHREYER HONORS COLLEGE

DEPARTMENT OF MECHANICAL ENGINEERING

Effects of Aspect Ratio and Mass Distribution on Settling Cylinders

BRAYDEN BOWIE
SPRING 2022

A thesis
submitted in partial fulfillment
of the requirements
for a baccalaureate degree
in Mechanical Engineering
with honors in Mechanical Engineering

Reviewed and approved* by the following:

Margaret Byron
Assistant Professor of Mechanical Engineering
Thesis Supervisor

Daniel Cortes
Assistant Professor of Mechanical Engineering
Honors Adviser

* Electronic approvals are on file.

ABSTRACT

Particle-laden flows are widespread in nature, playing an important role in many processes including the global carbon cycle and the transport of pollutants. Naturally occurring aggregates are composed of complex geometries, which results in nonspherical particles with a center of mass (CoM) not located at the same location as the center of buoyancy (CoB). In this study, nonspherical particles were simplified to cylinders in order to investigate settling velocities and trajectories. Cylinders were 3D printed out of two materials: Polyethylene Terephthalate Glycol (PETG) and Acrylonitrile Styrene Acrylate (ASA). Utilizing 3D printing allowed for the CoM to be easily varied by changing the percentage of each material. Cylinder aspect ratios (AR) ranged from 1 to 4. The cylinders, with intermediate Reynolds numbers (Re) on the order of 100, were dropped horizontally into a tank of still (tap) water. The settling velocity and trajectories of the cylinders were recorded, and the orientations of the falling cylinders were qualitatively observed. Results demonstrated that 3D printed non-uniform display experimentally measured settling velocities close to theoretically predicted velocities, regardless of variations in mass distribution. Four different falling behaviors were observed: (1) vertical trajectory/horizontal-periodic orientation (2) vertical trajectory/vertical-periodic orientation (3) constant slanted trajectory and orientation and (4) periodic slanted trajectory and orientation. All cylinders, regardless of falling behavior and mass distribution, experienced the denser (PETG) material pointing downward. As AR increased, periodic oscillation in cylinder orientation increased. At a transitional state, cylinders no longer experienced these periodic oscillations and fell at a steady equilibrium angle. These results validate the use of material extrusion 3D printing

for future studies in the settling of CD cylindrical particles and have important implications for a greater understanding of naturally occurring nonspherical particles.

TABLE OF CONTENTS

NOMENCLATURE

Re = Reynolds Number

UD = Uniform Density

CD = Compound Density

CoM = Center of Mass

CoB = Center of Buoyancy

TEP = Transparent Exopolymer Particles

PETG = Polyethylene Terephthalate Glycol

ASA = Acrylonitrile Styrene Acrylate

STL = Stereolithography

AoS = Axis of Symmetry

LIST OF FIGURES

LIST OF TABLES

ACKNOWLEDGEMENTS

I would like to thank Dr. Margaret Byron for her guidance and providing me the opportunity to challenge myself as an undergraduate researcher. I would also like to thank the graduate students of the Environmental and Biological Fluid Mechanics Lab for their mentorship and their willingness to provide support. Finally, I would like to thank Casey Emler. The completion of this thesis would not have been possible without you holding me accountable and ensuring I met all of my writing goals.

Chapter 1

Literature Review

1.1 Particle in Nature

Particle laden flows frequently occur in nature, playing a key role in many processes such as the carbon cycle, sedimentation, and aerosols. When studying flows, it is easiest to assume particles as spheres in order to reduce the complexity of the equations that govern the particles' motion. Some particles of interest include naturally occurring organic particles known as marine aggregates [1]–[3] as well as microplastic pollution [4]. These are the two examples we will use to motivate our study of particles in flow. While some forms of microplastic may be spherical (e.g. microbeads), a majority of particles found in natural flows have irregular shapes with complex mass distributions.

Marine aggregates, or "marine snow", play an important role in our ecosystem. These slowly settling particles are responsible for about 40% of global primary production [5]. Marine aggregates that are not recycled in the upper 100m of the ocean can aggregate into larger marine snow particles. These particles play an important role in the carbon cycle by transporting carbon into deeper waters where sedimentation occurs. Marine snow particles are often greater than 0.5mm in length and are composed of several forms of organic and inorganic material, such as transparent exopolymer particles (TEP) secreted by bacteria and phytoplankton. TEP is a key method of transport for bacteria in the water to colonize solid particles [6]. The coagulation of these suspended particles leads to the formation of macroscopic aggregates [7]. These marine

snow particles are extremely delicate and are subject to forces that can either break them (disaggregation) or combine them with other particles (aggregation).

Constant disaggregation and aggregation of marine snow particles results in unique particle compositions. Marine snow particles have sizes ranging from microns to centimeters [3] as well as complex geometry and density distributions. These complex density distributions are a result of marine snow composition; organic particles such as carbon, fecal matter, soot, and living organism as well as inorganic particles such as microplastics and clay-materials [3]. These already complex geometries and mass structures may become increasingly complex due to constant disaggregation and aggregation. This creates situations where the center of mass (CoM) may not share the same location as the center of buoyancy (CoB). This may have implications on marine snow particles' settling velocity and trajectory at terminal velocity, making the approximation of marine snow particles as spheres not a good assumption. R.W Sternberg et al. showed that approximating marine snow as spheroids rather than spheres resulted in a 13% difference in computed settling velocity of marine snow [8]. By using an spheroidal approach, predicted data matched experimental data with higher accuracy.

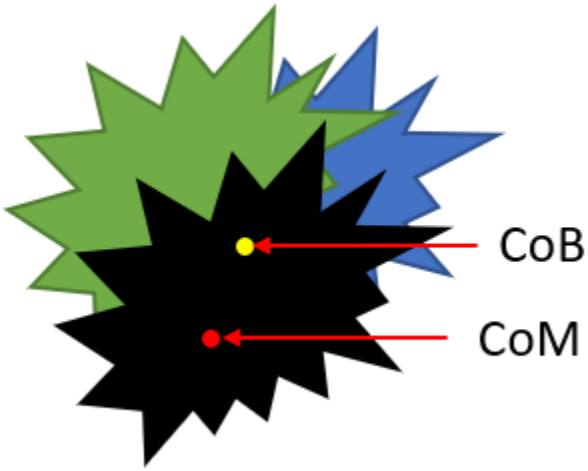

Figure 1. A nonspherical particle where each color represents a different density particle. The CoM of this complex particle is not collocated with the CoB due to the uneven mass distribution of the particle.

1.2 Non-spherical Particles with Varied Center of Mass

The Reynolds number (Re) represents the ratio of inertial forces to viscous forces experienced by a settling particle. The Re can be defined as:

$$Re = \frac{\rho v d}{\mu} \tag{1}$$

where ρ = density, v = velocity, d = diameter, and μ = viscosity. However, predicting the settling velocities of particles at intermediate Re pose several challenges. A particle falling through a still moving fluid is subject to the force of gravity, as well as forces exerted by the fluid such as buoyancy and drag. At low Re, fluid drag is linearly proportional to settling velocity as predicted by the Stokes flow assumption. However, at finite Re, inertial effects are

large enough that they cannot be ignored, increasing the complexity of the Navier-Stokes equation. This results in a fluid drag force that is nonlinearly proportional to velocity.

Particles with uneven mass distributions experience different settling behaviors than uniform density particles. Uneven mass distribution impacts a particles trajectory and falling behavior, resulting in difficulties in predicting settling behaviors of these particles. Falling cylinders with uneven mass distributions experience complex downward trajectories as they fall [9]. Previous work found that when the cylinder's CoM was co-located with the CoB, cylinders fell near the drop point more than 90% of the time. Slightly moving the CoM led to variabilities in settling trajectories. The CoM/CoB location had a greater influence on the cylinder's landing site than the initial drop angle of the cylinder, which ranged from 15 degrees to 75 degrees and the cylinders aspect ratio (AR). The CoM/CoB location also has an impact on the cylinders falling orientation. Compound density (CD) cylinders have been shown to fall in several distinct orientations, including a constant horizontal orientation, slanted orientation, or oscillations about a stable angle [10].

Early models first attempted to gain an understanding of inertia effects on long slender bodies. In their development of the finite Re slender body theory, Khayat and Cox analyzed how weak fluid inertia, which is present at Re that are not significantly greater than one, affects the settling of a long slender body [11]. Their analytical model accurately showed the relationship between Re and the force of drag of slender bodies. They also noted that a horizontal falling orientation is the only stable steady state falling orientation for a slender body. However, since natural particles don't often take the form of a sphere with a uniform mass distribution, the behavior of particles with the CoM not at the object's centroid (that is, not at the CoB) relevant to our motivating applications must be investigated. Candelier and Mehling extended Khayat and

Cox's slender body approximation, examining a dumbbell shaped particle composed of two spheres of the same mass density connected by a massless rod [12]. As shown in Figure 2, they determined that when δb (the difference in diameter between the two spheres) is large, an asymmetric dumbbell tends to settle vertically with the larger sphere below the smaller one. However, when the Re is small but finite, and there exists a small asymmetry in the dumbbell, this is not the case. There exists a steady state falling angle in which the effects of the geometric asymmetry are balanced by the force due to fluid inertia. At this finite Re, even a large δb does not guarantee a vertical falling orientation.

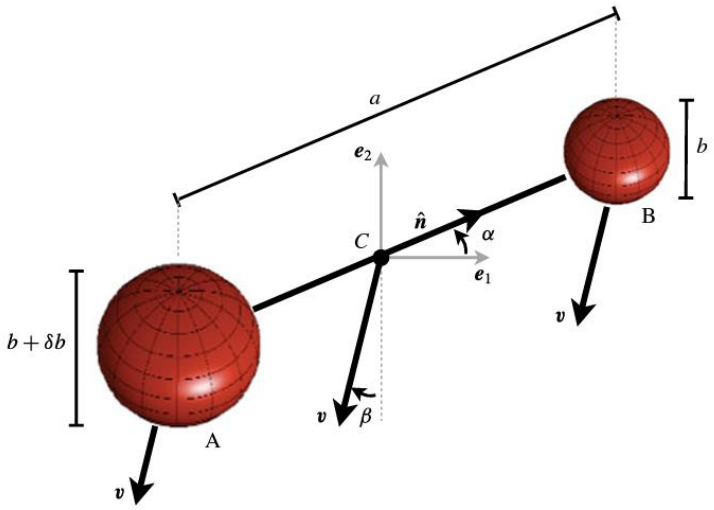

Figure 2. Illustration of dumbbell shaped particle connected by a massless rod, reproduced from Candelier and Mehling [10].

Since Khayat and Cox performed their initial fluid inertia calculations of forces on slender bodies, there have been many qualitative observations to validate these findings, but development of accurate models has proven difficult [13]. At high Re, particle trajectories can accurately reproduce the findings of Khayat and Cox. However, at low Re and high AR,

imperfections in experiments can strongly influence results since the effects of fluid inertia are small. This results in a need for increased study of nonspherical particles with asymmetry. Roy et al. provided experimental measurements of the drag forces and internal torques acting on asymmetric fibers [13]. They showed that at finite Re, asymmetric fibers experience competing torques from fluid inertia, gravitational forces, and viscous forces. Inertial forces favor a horizontal settling orientation while gravitational forces favor a vertical settling orientation with the heavier side landing first. Gravitational forces pull the heavier side of the fiber towards a vertical orientation with inertial forces provide a competing force attempting to gain a horizontal orientation. At finite Re, a very small asymmetry (that is, a very small offset between the CoM and the CoB) was found to have a dramatic impact on the settling orientation, showing that a particle's mass distribution plays a crucial role in determining particle settling orientation. Natural particles do not always take on the shape of asymmetric fibers. This motivates the need to validate slender body models with nonspherical particles of low AR at transitional Re.

1.3 Kinematics and Dynamics of Settling Velocity

Marine snow plays an important role in the global carbon cycle, and understanding its settling velocity allows for greater understanding of carbon sedimentation in deep ocean waters. A particle reaches terminal settling velocity when the gravitational force is balanced with fluid drag. The settling velocity of a particle is influenced by a variety of geometric and hydrodynamic parameters. For nonspherical particles settling at finite Re, we rely on a combination of analytically and experimentally derived drag coefficients to predict what the settling velocity will be. Formulas that were originally derived for spherical particles can be adapted to represent non-

spherical particles, such as spheroids, in order to predict settling velocity [13]. Spheroids can be defined as either prolate or oblate, with prolate spheroids having aspect ratios AR>1 and oblate spheroid having AR<1 (where the aspect ratio is the ratio of the major axis to the minor axis).

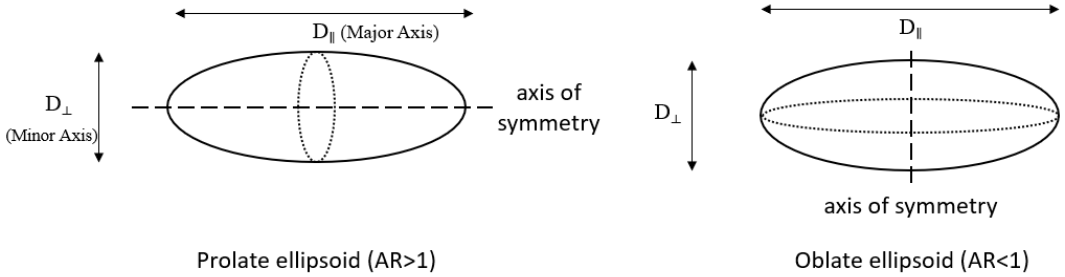

Figure 3. Defining the dimensions of a spheroid.

The particle Reynolds number (Re_p) characterizes important features of the drag the particle experiences as it settles. However, for a non-spherical particle, it is not always clear what the appropriate lengthscale (for defining Re_p) might be. A universal Re_p, defined for any shape, can be defined based on a sphere with equivalent volume to that of the initial particle:

$$Re_p \equiv \frac{\rho_f |w| d_{eq}}{\mu_f} \tag{2}$$

where $d_{eq} \equiv 2 \cdot \sqrt[3]{\frac{3}{4\pi} V}$ if V is the particle volume. There are several other methods to characterize an equivalent diameter other than the equivalent-volume approach. Many particles are irregular and do not resemble regularly shaped objects (such as a sphere, cube, or octahedron), and can be difficult or impossible to measure. The Corey shape function utilizes three lengths of a particle in mutually perpendicular directions to characterize irregular particles [14] by measuring the particles longest dimension, shortest dimension, and intermediate dimension. These dimensions are obtained from visualizations above and from the side of a

particle. These dimensions are repeated for a statistically large number of samples, allowing an average max-med-min area to be obtained. While effective at characterizing irregular particles, it is time consuming. It is recommended to use only a sphericity approach (creating a sphere with an equivalent surface area) when possible since particles trajectories may include secondary motion, resulting in falling orientation that is not always horizontal [14].

The equations for the drag force on a sphere can be adapted for a cylinder, where (again) the diameter used is that of a sphere with equivalent volume. Cylinders are nonspherical particles that provide a simplification of marine snow particles: they are easier to manufacture while having similar shape to spheroids. This allows us to apply drag approximations)originally defined for spheres) to a cylinder. The accuracy of this approximation can be further improved by using a shape correction factor. With this approximation, the drag force in Stokes regime, where $Re_p << 1$, is defined as shown in equation 3. The drag force in Newton regime, where $Re_p >> 1$, is defined as shown in equation 4.

$$F_D = -3\pi d_{eq}\mu_f v \tag{3}$$

$$F_D = -\frac{\pi}{8} {d_{eq}}^2 \rho_f C_D v^2 \tag{4}$$

Equation (4) can also be used for $Re << 1$ using the drag coefficient $C_D = \frac{24}{Re} = \frac{24\mu}{\rho_f v d_{eq}}$. At low Re, the drag force is linearly proportional to the velocity; at high Re, it is proportional to the velocity squared. At intermediate Re, the drag force is proportional to v^n where $1 < n < 2$. This is expressed by using Equation (4) with a drag coefficient C_D which is dependent on the particle Reynolds number. For the intermediate Re case, C_D can be defined with a drag correction factor given by Clift and Gauvin [15], as shown in equation 5:

$$C_D = \left[\frac{24}{Re_p}\left(1 + .15Re_p^{.687}\right)\right] + \frac{.42}{1 + \frac{42{,}500}{Re_p^{1.16}}} \quad (5)$$

However, this correction factor is one of many possible approaches, and was originally derived only for spheres. Determining a robust dependency between Re and the drag coefficient has proved difficult for nonspherical shapes. Ganser and Cheng [15], [16] normalized the drag coefficient and Re with shape correction factors,

$$C_D{}^* = \frac{C_D}{C_{shape}} \quad (6)$$

$$Re_p{}^* = \frac{C_{shape} Re_p}{f_{shape}} \quad (7)$$

where both C_{shape} and f_{shape} are dependent upon the aspect ratio AR of the cylinder. For AR < 1, C_{shape} and f_{shape} are defined by equations 8 and 9. Equations 10 and 11 define C_{shape} and f_{shape} for AR >1.

$$C_{shape} = 1 + 1.5\sqrt{(A_{surf}{}^* - 1)} + 6.7(A_{surf}{}^* - 1) \quad (8)$$

$$f_{shape} = \frac{AR^{\frac{-1}{3}}\sqrt{1 - AR^2}}{cos^{-1}AR} \quad (9)$$

$$C_{shape} = 1 + 1.7\sqrt{(A_{surf}{}^* - 1)} + 2.4(A_{surf}{}^* - 1) \quad (10)$$

$$f_{shape} = \frac{AR^{\frac{-1}{3}}\sqrt{AR^2 - 1}}{\ln\left(AR + \sqrt{AR^2 - 1}\right)} \quad (11)$$

In these expressions, $A_{surf}{}^*$ is the normalized surface area with respect to a sphere of equivalent volume and defined in equation 12:

$$A_{surf}{}^{*} = \frac{A_{surf}}{\pi d_{eq}{}^{2}} \quad (12)$$

1.4 Cylinder Fabrication

There have been numerous approaches to manufacture compound density (CD) cylinders with adequate geometric tolerances. One approach is to create particles from a glass capillary tube filled with ultra-violet curing optical glue [13]. In order to create asymmetry, air bubbles are introduced on one side of the tube. The use of a glass capillary tube allowed for a very high-quality surface finish that would not affect sedimentation, but the transparency of the glue led to difficulties with imaging the tube. Another approach is to machine cylinders. Surface roughness can significantly impact the dimensional behavior of a particle. Previous work by Bagheri et al. compared irregularly shaped volcanic particles to inscribed and circumscribed volcanic particles (achieved through machining processes); results showed that, reducing surface roughness caused particles to experience higher terminal velocities and decreased drag forces. [16]. While machined parts are able to achieve low surface roughness, machining small particles is both difficult and expensive due to the high precision machinery required. Recently, hydrogels have been used to create “compound density” cylinders, made of piecewise-varying-density segments, where the density of each segment can be precisely controlled [14].

With the advent of additive manufacturing, this method has become an option for fabricating nonspherical particles with nonuniform mass density. However, there are also some limitations. While printers such as material extrusion and photopolymerization are rather inexpensive, printers with fine geometrical tolerances are expensive. Roy et al. (2019), determined that 3D printing with a Form1+ photopolymerization printer from Formlabs was

inappropriate [13] for slender bodies, because the surface roughness due to 3D printing was large enough to substantially effect the settling of particles. This raises the general issue of the surface resolution needed to conduct experiments with falling particles, and when surface roughness may affect the variables we are interested in measuring. The Form 3+ is Formlabs 3rd generation resin-based printer, which has a resolution as low as 25μm [17], compared to traditional material extrusion-based 3D printers have a resolution as low as 50μm. In order to achieve lower surface roughness values that are similar to that of a machined cylinder or a glass capillary tube, a material jetting printer, which has a resolution as low as 15μm [18], must be used. However, material jetting printers are costly. In a 2017 study, Chaudhari et al. showed that traditional material extrusion 3D printed parts can be smoothed via vapor treatment with acetone. This smoothing process is able to improve surface roughness of 3D printed parts by almost four times, producing a finer surface finish than that of a material jetting process [19]. This could be a potential way to alleviate surface roughness concerns and use 3D printing for the study of nonspherical nonuniform particle settling. It is currently unclear if particles at lower AR will be affected by surface roughness due to 3D printing as previously seen in slender bodies.

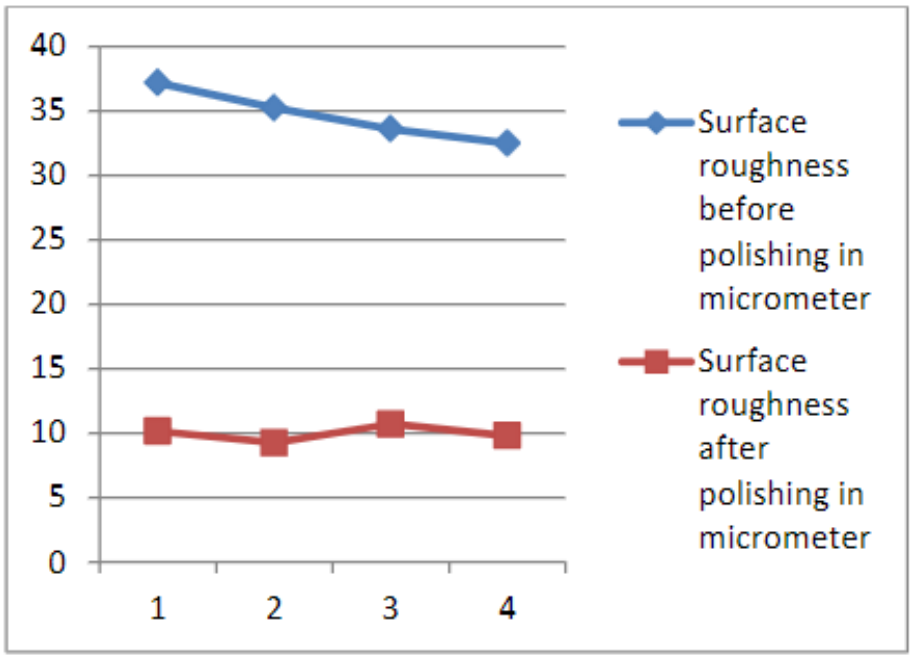

Figure 4. On the Y axis of the graph, values of surface roughness are measured in micrometers. The X axis of the graph shows the number of specimens examined. Reproduced with permission from Chaudhari et al (2017) [19].

1.5 Research Goal

The goal of this thesis is to gain a greater understanding of the settling behavior of cylinders of unequal mass distribution where the CoM is not located at the CoB. It continues previous work by Brandon Angle in which he studies the settling behavior of uniform *vs* compound-density hydrogel cylinders [10].

Previous work showed that cylinder AR and density distribution was correlated to settling behavior. Cylinders fell with three behavior modes:

- Mode 0 cylinders fell with a vertical trajectory and fell in a horizontal orientation.
- Mode 1 cylinders fell with a slanted trajectory in a stable, angled orientation.

- Mode 2 cylinders fell with a vertical trajectory, but oscillated about a vertical orientation as they fell.

In this previous study, UD cylinders fell in either Mode 0 or Mode 2, with AR being the primary factor impacting the falling orientation. CD cylinders never fell in Mode 0, but did fall in Modes 1 and 2. A small group of cylinders were observed transitioning from Mode 1 to Mode 2, however, mechanisms underlying this transitions were unclear. He hypothesized that the cylinders were falling very close to some critical Reynolds number threshold, so that small differences in manufacturing or fluid viscosity would change the falling orientation (by slightly changing the Re). He provided evidence for this hypothesis by using temperature to change in the viscosity of the water, which substantially affected cylinder settling velocity for some cases.

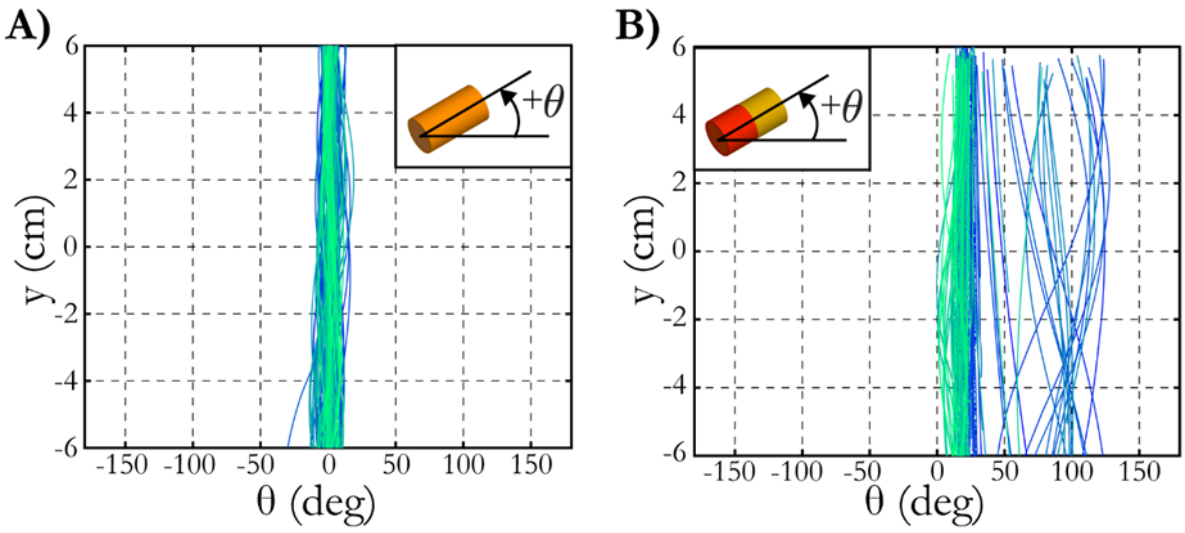

Figure 5. Major axis orientation for (A) UD cylinder AR = 2 and (B) CD cylinder AR = 2. Reproduced with permission from Angle (2019) [10]

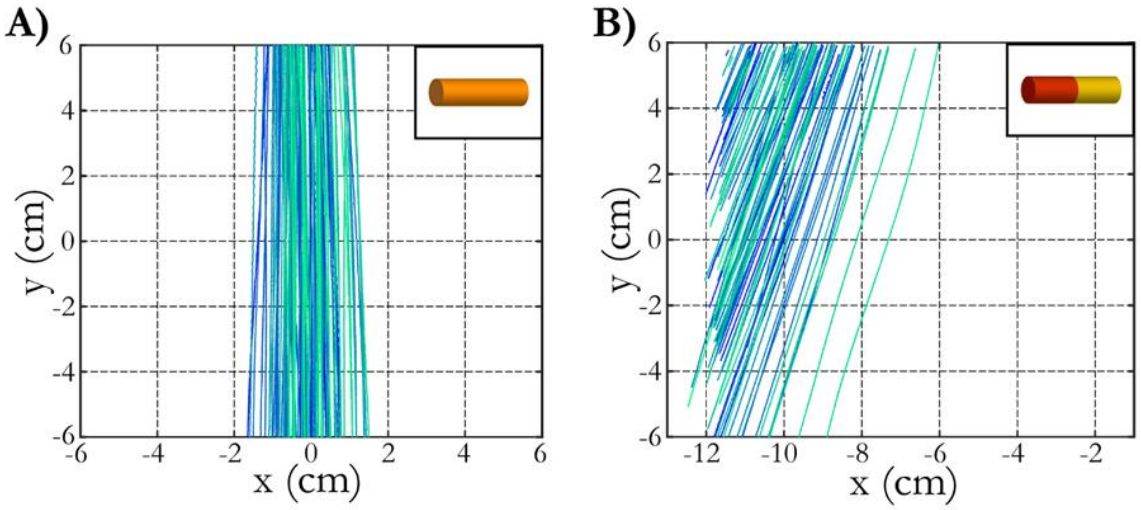

Figure 6. Trajectories of (A) UD cylinders AR = 4 and (B) CD Cylinders AR = 4. Reproduced with permission from Angle (2019) [10]

The correlations between settling behavior, AR, and density distribution (and the fluid dynamic mechanisms that determine the falling modes) are still not well understood. Angle's work used cylinders with an approximate Re_p of 210 which is a transitional Re for the wakes of spheres and cylinders [20]. At this transitional Re, flow surrounding the cylinder becomes unsteady as the wake becomes detached. The flow becomes more unstable as Re increases, and regions of high vorticity are created in the wake of the cylinder. In Angle's study, CD cylinders were composed of equal parts of each density (that is, two halves, each with one uniform density). Rather than creating a cylinder that is half one density and half another, we will vary the composition, which may provide more insight into how density distribution impacts settling behavior. This will be accomplished by creating cylinders that have additional compound density arrangements of unequal parts of two different uniform density materials. This change in composition will move the CoM to locations that were not considered in previous work.

In this thesis, cylindrical particles will be manufactured using 3D printing. Because cylinder dimensions are large (on the order of 4-30mm) compared to the printer resolution (on the order of 100 microns), we consider effects of surface roughness to be negligible and do not use any smoothing techniques as previously discussed. CD cylinders will be composed of PETG and ASA. These materials were selected due to their ability to create waterproof prints (preventing waterlogging and accompanying density changes), similar printing temperatures, and the large density difference between them. The advantages of 3D printing, as discussed in the previous section, are that particles can be quickly printed, reproduced with high accuracy and are easy to manufacture at a low cost. Materials have a known density, allowing for particles to be designed at (predictable) intermediate Re in order to gain a greater understanding of how a nonuniform density distribution affects a particle's settling velocity and orientation. This thesis will explore these effects over a wide range of cylinder aspect ratios and density distributions.

Chapter 2

Methods

2.1 Cylinder Design Process

To ensure that our experiments are relevant to our two motivating cases (marine snow and microplastics), we choose a target Re of approximately 200 based on the particle's settling velocity and its volume-equivalent sphere diameter d_{eq} (the diameter of a sphere with the same volume). Marine snow and microplastics can have complex shapes (such as fractal geometries) [21]; to simplify the problem, while still maintaining ease of manufacturing and the ability to vary particle aspect ratio (AR) in a well-defined way, we choose to perform our experiments with cylinders. Cylinders are nonspherical; we approximate them as spheroids to take advantage of established empirical expressions for the drag coefficients of spheroids at intermediate Reynolds numbers [14] (see Chapter 1.3). This allows us to predict the terminal settling velocity of cylinders with known aspect ratio and (uniform) mass density. Marine snow particles have Re on the order of 10^{-1} to 10^{2}. Previous work on cylinders settling around this Re has shown that compound density (CD) cylinders—those whose mass density varies along their length—have nontrivially different settling behaviors compared to uniform density (UD) cylinders [10]. However, this previous study only varied the AR and did not consider how the relative location of the center of mass (CoM) within the cylinder impacts settling behaviors.

In this study, we vary the CoM location by varying the density distribution of cylinders of different aspect ratios. Each cylinder is bipartite, with piecewise density variation between two available densities ($\rho_1 = 1.27 g/cm^3$ and $\rho_2 = 1.07\ g/cm^3$). We consider three different cases:

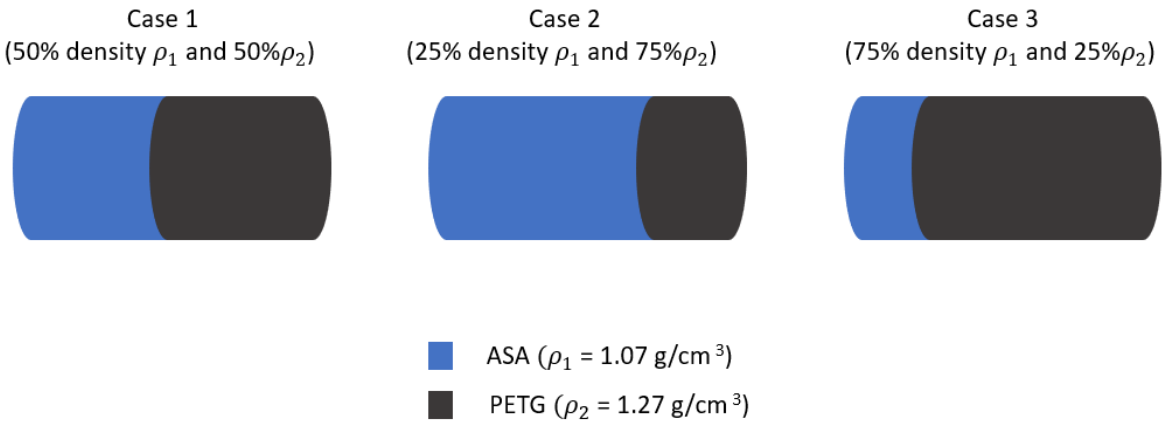

Figure 7. Mass distribution cases (Case 1, Case 2, Case 3). The blue cylinder represents ASA and the black cylinder representing PETG with respective densities of ρ_1 = 1.07 g/cm^3 and ρ_2 = 1.27 g/cm^3.

As discussed in Chapter 1, we use 3D printing to fabricate the cylinders with two different materials (with densities ρ_1 and ρ_2 shown in Figure 7). The materials used must have similar printing parameters in order to ensure good cohesion between the two materials. We therefore use polyethylene terephthalate glycol (PETG) and acrylonitrile styrene acrylate (ASA) as material 1 and 2 respectively. As stated above, PETG has a density of 1.27 g/cm^3 and ASA has a density of 1.07 g/cm^3. PETG requires a nozzle temperature of 250 °C ± 10 °C and a heatbed temperature of 80 °C ± 10 °C. Similarly, ASA requires a nozzle temperature of 260 °C ± 10 °C with a heatbed temperature of 110°C ± 10 °C.

The cylinders must be large enough to easily image their settling behavior with high-speed videography while also maintaining the desired Re. Because the choice of materials (and therefore the cylinder density) is constrained by the manufacturing method, the size of each cylinder is the only variable that can affect the settling velocity (and therefore Re). We are free

to set the diameter, length, and composition (distribution of ρ_1 and ρ_2 material) in order to achieve our desired Re at several different aspect ratios.

Predicting the settling velocity of a nonspherical particle falling at intermediate Re is not straightforward. While we can predict the gravitational/buoyant forces directly from the geometry and particle/fluid densities, the drag force on such a particle is nonlinearly related to the settling velocity (and the drag coefficients are themselves a function of the Reynolds number). The orientation in which the particle falls also affects the drag force. However, to assist in designing the cylinder geometry, we conduct a "first pass" approximation of the predicted settling velocity by iteratively solving the force balance on the cylinder.

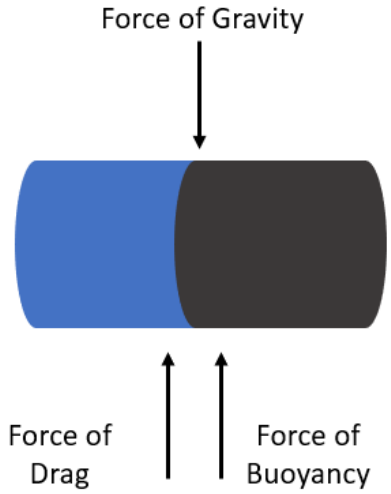

Figure 8. Free body diagram of the forces on a CD cylinder. For the particle to reach terminal velocity, the force of gravity minus the force of buoyancy must be equal to the force of drag.

In order to calculate the cylinder geometry that should yield the desired Re during settling, we created a MATLAB script to automatically iterate the design (see Appendix A). This program utilizes Equations 1-12 (from [14]) to approximate the cylinder as a spheroid with a

uniform density (the average density for each case), with dimensions a, b, and c of the spheroid being matched to the cylinders radius and length as shown in Figure 9. The script requires three inputs: diameter, length, and an initial terminal velocity prediction. The user can manually manipulate the cylinder dimensions until the desired Re is reported in the command window. Terminal velocity must be calculated iteratively until that condition is met. The terminal velocity prediction will be automatically iterated by MATLAB; at each iteration step, it adjusts the values of the drag coefficients, shape factors, and other parameters which depend on the velocity. The script continuously adjusts the velocity prediction until the net gravitational force and (calculated) drag force are equal and opposite, and outputs the final Re (based on this velocity) to the command line. The user can modify the initial dimensions of the cylinder in order to achieve any desired Re, as long as the predicted Re is within the range that is appropriate for Equations 2-12.

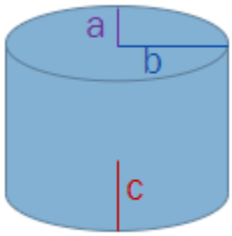

Figure 9. Approximating a cylinder as a spheroid with dimensions a and b representing the cylinder radius, and dimension c representing half of the cylinder height.

In general, it is more desirable to slightly under predict Re rather than over predict; previous work found that experimentally measured Re tend to be larger than the Re predicted using this method possibly due to the increased surface area a cylinder has to spheroids of the same dimension [10]. We also hypothesize error of up to 10% in the prediction of Re because we

approximate the cylinders as spheroids. In the application of this approach to disks, an error of up to 14% was observed when compared to the exact solution [14]. Tables 1-3 below contain cylinder dimensions as defined by Figure 9 as well as the predicted Re for each density case with 5 different AR.

Lastly, we note that prior to determining all cylinder dimensions for this study, we produced multiple UD cylinders printed with Polylactic Acid (PLA), a material which has a density between that of PETG and ASA. These cylinders were used to narrow the range of dimensions that would be appropriate for the experimental setup (and feasibly produced by the 3D printer) and ensure that the camera field of view was appropriately set. Four AR 2 PLA cylinders with diameters of 1 mm to 7 mm were printed and dropped in the test tank described in section 2.3, covering the range of sizes we considered for CD cylinders. These results (not reported here) guided the selection of a 55mm macro lens would provide an appropriate FOV for the experiments, and revealed that the CD cylinders used in experiments should not have a dimension smaller than 1mm for ease of imaging.

Table 1. Cylinder design for Case 1 (50% density ρ_1 and 50%ρ_2).

Aspect Ratio	a (mm)	b (mm)	c (mm)	Predicted Reynolds Number ± 14%
1	2.75	2.75	2.75	208
2	2.40	2.40	4.80	205
4	2.15	2.15	8.60	209
6	2.00	2.00	12.00	203
8	1.95	1.95	15.60	206

Table 2. Cylinder design for Case 2 (25% density ρ_1 and 75%ρ_2).

Aspect Ratio	a (mm)	b (mm)	c (mm)	Predicted Reynolds Number ± 14%
1	2.75	2.75	2.75	207.99
2	2.7	2.7	5.4	205.13
4	2.4	2.4	9.6	206.37
6	2.25	2.25	13.5	203.33
8	2.2	2.2	17.6	207.77

Table 3. Cylinder design for Case 3 (75% density ρ_1 and 25%ρ_2).

Aspect Ratio	a (mm)	b (mm)	c (mm)	Predicted Reynolds Number ± 14%
1	2.75	2.75	2.75	207.99
2	2.2	2.2	4.4	203.98
4	1.95	1.95	7.8	204.38
6	1.85	1.85	11.1	205.46
8	1.8	1.8	14.4	208.26

2.2 Cylinder Fabrication

As discussed in section 1.4, 3D printing allows for rapid, repeatable, and convenient manufacturing of cylinders with a precise geometry and density distribution. In previous studies, it has been noted that the surface roughness of 3D printed particles was potentially large enough to impact settling behaviors [13]. Therefore, the effect of surface roughness should be considered

in our study. We note that the majority of previous studies, of falling cylinders at low or intermediate Re considered slender bodies [10]–[13], [21], [22] with much higher AR than what we seek to examine here. Because this study focuses on lower AR, ($1 < AR < 8$), the effects of surface roughness are less important due to decreased drag force. We therefore choose to use a material extrusion printer, the Prusa i3 MK3S+ (Prusa Research, Prague, Czechia). This printer has a significantly lower initial cost and increased ease of use compared to higher-end, higher-resolution filament or resin printers, while still producing prints of high quality. Additionally, this printer can be fitted with a multi material upgrade (MMU) that allows the printer to create objects composed of up to five different materials. This is a crucial function for our study, as many material extrusion printers can only print parts composed of one material. The MMU allows for parts to be printed as a single piece, eliminating the need to join two separate parts together to create CD cylinders.

We used Solidworks (Dassault Systèmes, Waltham, MA) to geometrically model all cylinders and output their dimensions as stereolithography (STL) files. To create a part that would be identified by the printer as multimaterial, CD cylinders were created as independent extrusions in a Solidworks part file and saved as separate STL files. The two STL files were then reassembled in a slicing software. Slicing software allows the printer to take STL files and convert them into a programming language called geometric code (commonly known as G-code). G-code gives a 3D printer instruction on a variety of printing parameters, such as nozzle temperature, heatbed temperature, coordinate locations for material deposition, and motor speed.

The Prusa printer will accept G-code from any slicing software, but we used PrusaSlicer for this experiment due to its ease of use and optimization for the Prusa printer. By inserting the two STL files (representing the two components of the CD cylinders) into the slicer at the same

time, we communicated to the printer that the cylinder is one continuous part composed of two different materials. In order to reduce surface roughness, we used the maximum “detail printing” setting with a resolution of .10mm. A skirt and brim were only used for cylinders with AR of 6 and 8 in order to provide stability when printing. Part density was set to 100% with a rectilinear infill pattern. To ensure consistency, each aspect ratio was printed three times in order to account for possible printing variations due to changes in temperature or humidity. These environmental changes can impact the cooling rate of the filament and may lead to minor part variations. PETG adheres to the (heated) build plate significantly more than ASA, therefore we set the print so that the PETG side of each CD cylinder was always touching the hot plate.

2.3 Experimental Setup

For this experiment, we constructed a rectangular water tank with dimensions of 5.375 inches by 5.375 inches by 30.5 inches and filled it with fresh (tap) water. Mounted to the top of the tank is a 3D printed platform that holds an Arduino Uno (Arduino, Sommerville, MA), a breadboard, and a robot claw (Gripper Robotics Kit from Kitronik Ltd, Glaisdale Point, Nottingham). The robot claw is centered over the tank. The robot claw consists of a gear attached to a servo motor wired to an Arduino Uno. The claw opens and closes based on the state of a push button located on the breadboard. Cylinders are placed in the claw, then released from the claw when the button on the breadboard is pressed. This allows for repeatability, ensuring that cylinders are dropped in the same orientation (loaded horizontally into the claw) and from the same height with the same initial conditions in every trial, removing potential human error from

the dropping process. This includes always loading the PETG side of the CD cylinder on the left of the robot claw as shown in Figure 10.

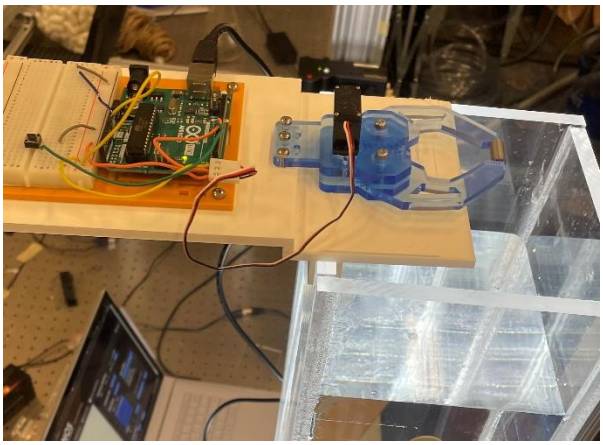

Figure 10. Robot Claw and electronics centered over tank via 3D printed base. Shown is a uniform density cylinder used in initial trials to determine FOV.

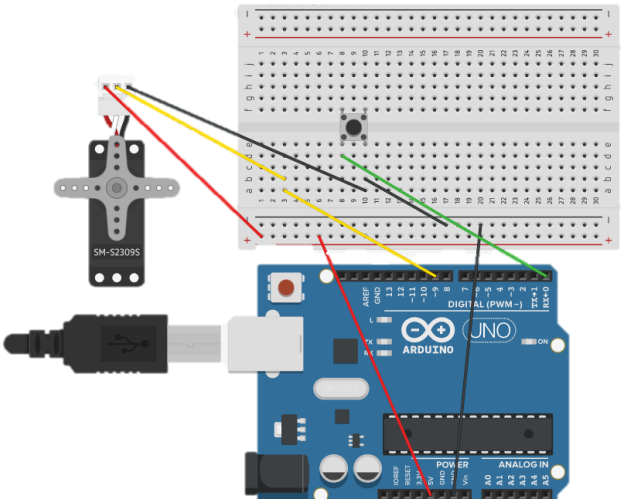

Figure 11. Wiring schematic of robot claw. Schematic created using Tinkercad (AUTODESK, San Rafael, CA)

Two high speed Chronos 1.4 (Krontech, Burnaby, BC, Canada) cameras are mounted 31.5 inches from the central (long) axis of the tank, offset from one another by at 90 degrees in order to capture three-dimensional cylinder motion. For consistency, the cylinder is always

loaded into the robot claw so that the denser (PETG) side is initially in the left of Camera 1's FOV. Videos were taken at a resolution of 1024x1024 at 500fps on each camera. Cameras recorded continuously into a ring buffer and were synchronized to ensure that frames started and ended at the same time. Videos were end-triggered with a BCN push-button switch. This prevented the need for post processing of videos to ensure that the frames of the separate videos coincide. Camera 1 has a 55mm f/2.8 Micro NIKKOR lens (Nikon, Minato, Japan) and Camera 2 has a 60mm f/2.8 Micro NIKKOR lens (Nikon, Minato, Japan). The difference in lens focal length is accounted for during camera calibration. The test sections (image area) of the tank were backlit by two diffuse LED panels (Charmax, Carrollton TX). Both LED panels were positioned behind the tank perpendicular to the optical axis of each camera, to illuminate the field of view and create contrast against the dark particles to perform later image processing on the captured videos.

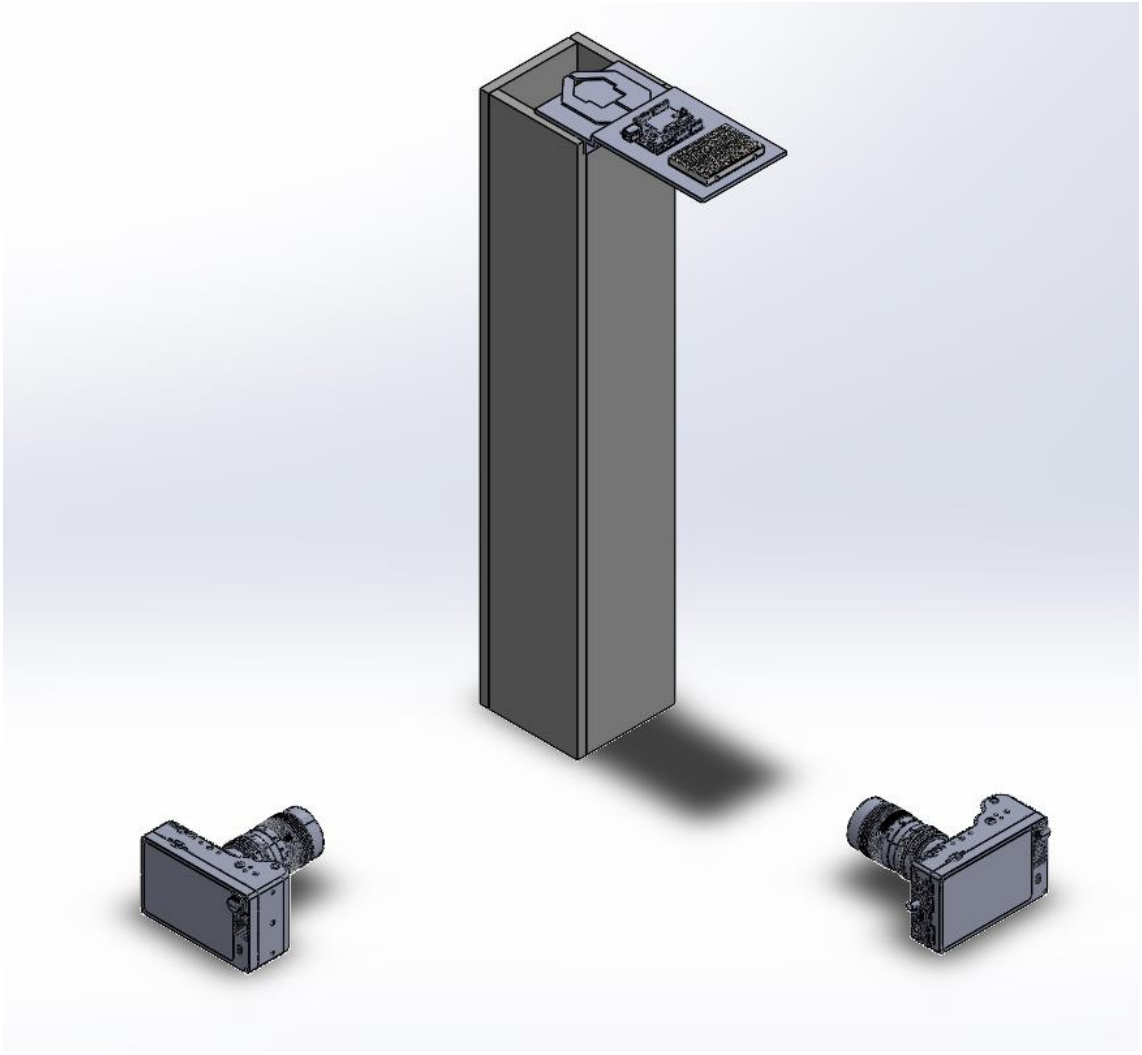

Figure 12. Experimental setup showing two Chronos 1.4 cameras position towards a still (tap) water tank. Mounted at the top of the tank includes a 3D printed stand, supporting a robot claw dropping mechanism powered by an Arduino Uno.

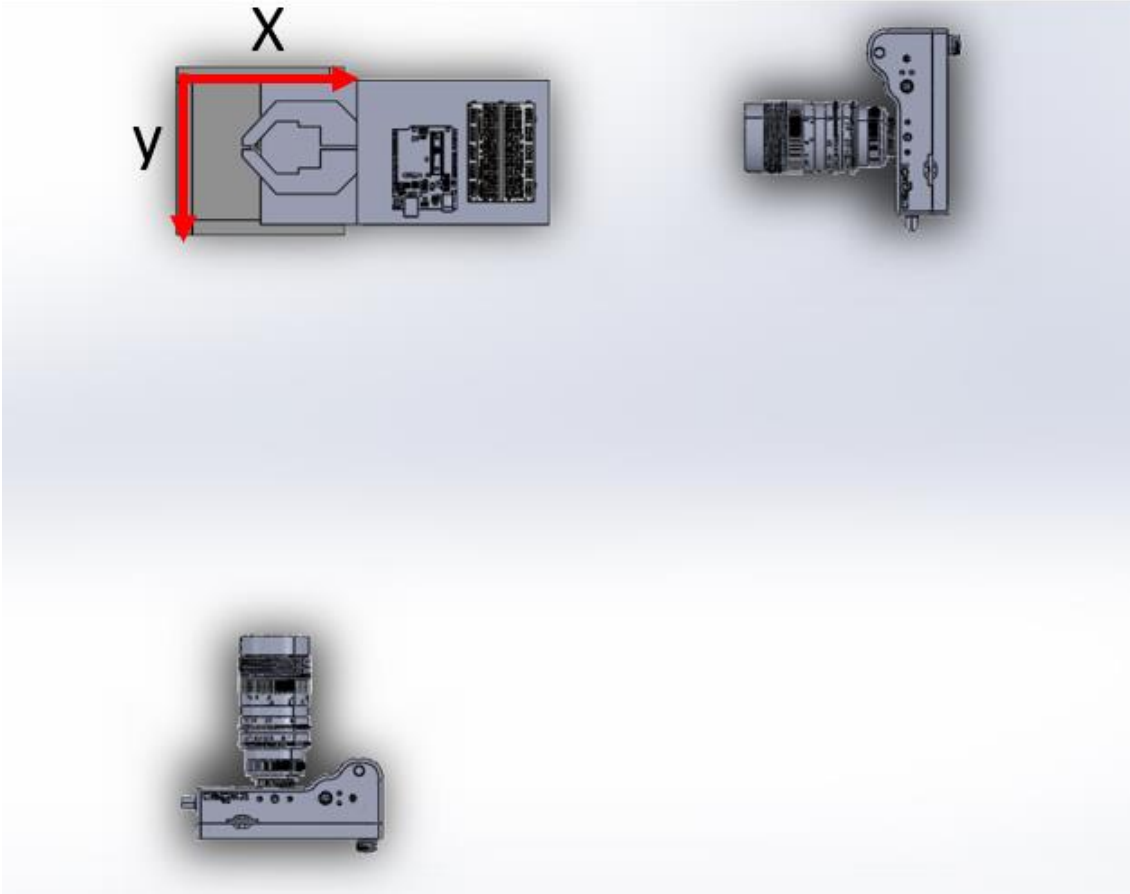

Figure 13. Top view of experiment setup showing two Chronos 1.4 cameras position towards a still (tap) water tank. Mounted at the top of the tank includes a 3D printed stand, supporting a robot claw dropping mechanism powered by an Arduino Uno.

2.4 Camera Calibration

To analyze the settling behaviors of the cylinders, the two camera views must be calibrated in 3D space. To accomplish this, we printed a checkerboard pattern on a piece of paper and secured it to a sheet of acrylic with transparent packing tape. This waterproofed the paper checkerboard without distorting the image (which would impact the calibration).

Prior to recording videos every day, the calibration plate is suspended in the tank by hand so that the checkerboard is visible in both cameras. The exact angle the plate makes with the two

cameras' optical axes is not important, but it is important that both cameras are able to see all of the squares on the checkerboard at all times. To start, the plate was angled at about 45 degrees to both cameras. We record two synchronized videos in which the calibration plate is moved horizontally and vertically in the tank, but not significantly rotated. In MATLAB, the corners of the checkerboard are identified and tracked using the built-in command *detectCheckerboard*. Wand points (a set of digitized points with 2 points marked per camera where each of the two points is one end of an object of known length) and background points (unpaired scene points) are saved into an Excel file. Using the MATLAB add-in EasyWand [23], we can calculate the Direct Linear Transformation (DLT) coefficients [24]. This add-in takes as the input the (previously generated) wand points and background points from the checkerboard videos, as well as the image sizes, focal lengths, and wand span (length of the calibration wand). To have a valid calibration, a "wand score" less than 1 must be achieved, indicating that there is little error in wand tracking. A large wand score will result in large reprojection errors (difference between points' calculated 3D position and their marked position on images) and incorrect image processing.

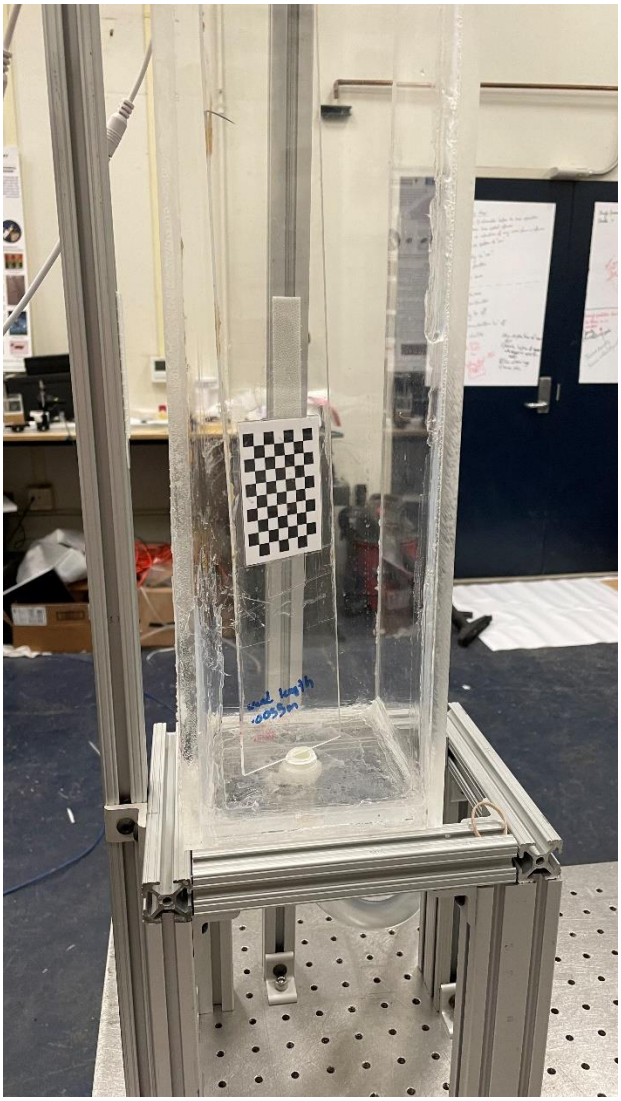

Figure 14. Calibration plate inside of tank. For calibration, the plate is moved (by hand) vertically and horizontally. The tank is filled with tap water, and the plate is slightly angled so that both cameras can view the plate.

Once calculated with a satisfactory wand score, the DLT coefficients are used as input for the MATLAB add-in DLTdv8, a multi-featured open-source software that allows for three-dimensional object tracking (where 3D space is reconstructed using the Direct Linear Transformation)[25]. Using this add-in, we will track of cylinders in 3D space to measure key settling characteristics.

Chapter 3

Results and Discussion

3.1 Experimental Challenges

We created three printed cylinders for each cylinder type described in Tables 1-3 to explore the repeatability and accuracy of using 3D printing to study settling behavior of CD cylinders. Initially, we aimed to study AR of 1, 2, 4, 6, and 8. Cylinders of AR 1, 2, and 4 were able to be consistently 3D printed in all three mass distributions without any print failures. However, prints of AR 6 and 8 resulted in significant failures. All printing failures resulted during the printing of the second material (ASA). To achieve the lowest possible surface roughness, all cylinders were printed with their axis of symmetry pointing vertically. However due to the thin and tall nature of cylinders having AR = 6 and 8, these prints collapse towards end of the print. During the changing of filament material, small variations such as print layers shifting or a not perfectly level surface would lead to the collapsing of the print during the deposition of the second filament. In order to add support without increasing surface roughness, a brim, which improves bed adhesion and prevents warping by adding additional outlines around the part, was added to AR 6 and 8 prints. This allowed AR 6 cylinders to complete printing with less frequent failures. However, these prints had significant surface imperfections and were not considered successful prints, as the surface imperfections were likely to influence the settling behavior of the cylinders. All AR = 8 prints failed with and without a skirt applied. In order to complete successful prints, a supporting structure would have be designed to support the

cylinders. Since this would lead to increased surface roughness where supports are present, we did not include AR 6 and 8 cylinders in the study.

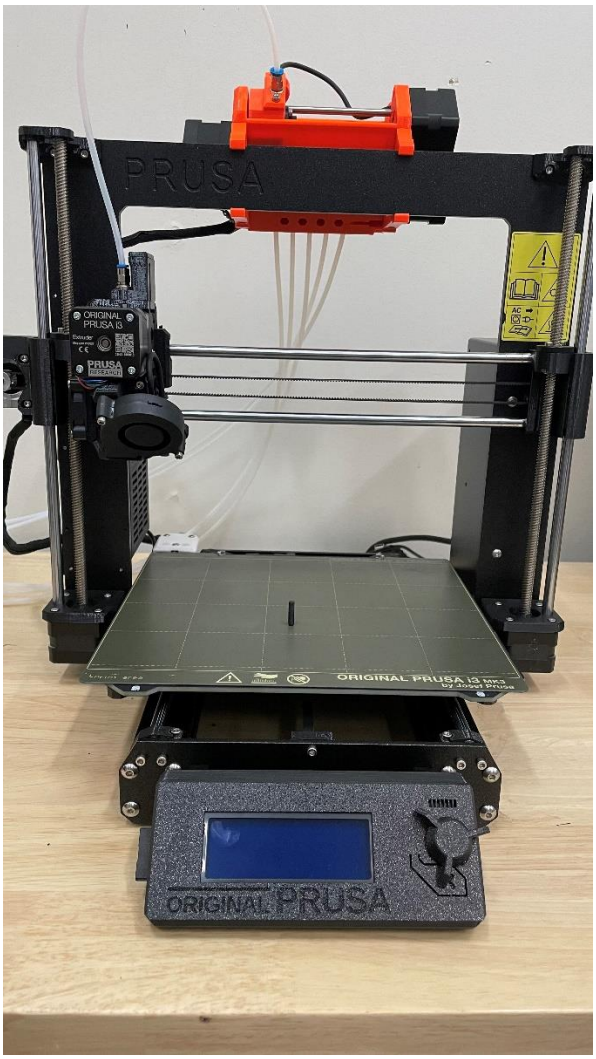

Figure 15. Prusa 3D printer. All cylinders are printed with the PETG filament touching the heatbed.

Figure 16. An example of a failed print. The layers began to shift when switching from PETG to ASA, resulting in increased surface roughness. The part finished printing, but the top of the part is extremely rough and uneven due. More extreme failure cases experienced ASA layers no longer adhering when layer shifting becomes too great.

Each of these three ARs were considered for three different mass distributions for a total of nine cases. Cylinders for each case were dropped into the settling tank three times. However, for some cases, the dropped cylinders did not pass the view field of the high-speed cameras. For these cases, an additional six drops were completed in an attempt to collect three experimental videos for analysis. If three successful videos (in which the cylinder passed through the view field of both high-speed cameras) were still not obtained after the additional drops, then less than three trials are available for this case. This occurred for case 1 AR = 4, and case 3 AR = 4. More information on the settling behavior that led to this situation can be found in Chapter 3.3.

3.2 Cylinder Settling Velocities

We measured settling velocities for the 3D printed cylinders that closely matched the predicted velocity for an spheroidal fit with similar dimensions. Figure 17 shows settling velocity as a function of AR for each of the three mass distribution cases as described in Chapter 2.1.

Because we chose the cylinder geometry to match the target Reynolds number of $Re = 210$, we predicted that for a given mass distribution, the settling velocity would not be impacted by AR. It was not clear *a* priori if this would be true for compound density cylinders; the drag model that we used was for a cylinder/spheroid of constant density. Our results show that the experimental and theoretical velocity predictions are roughly aligned for AR 1 and 2, regardless of mass distribution. However, for AR = 4, this is not always true.

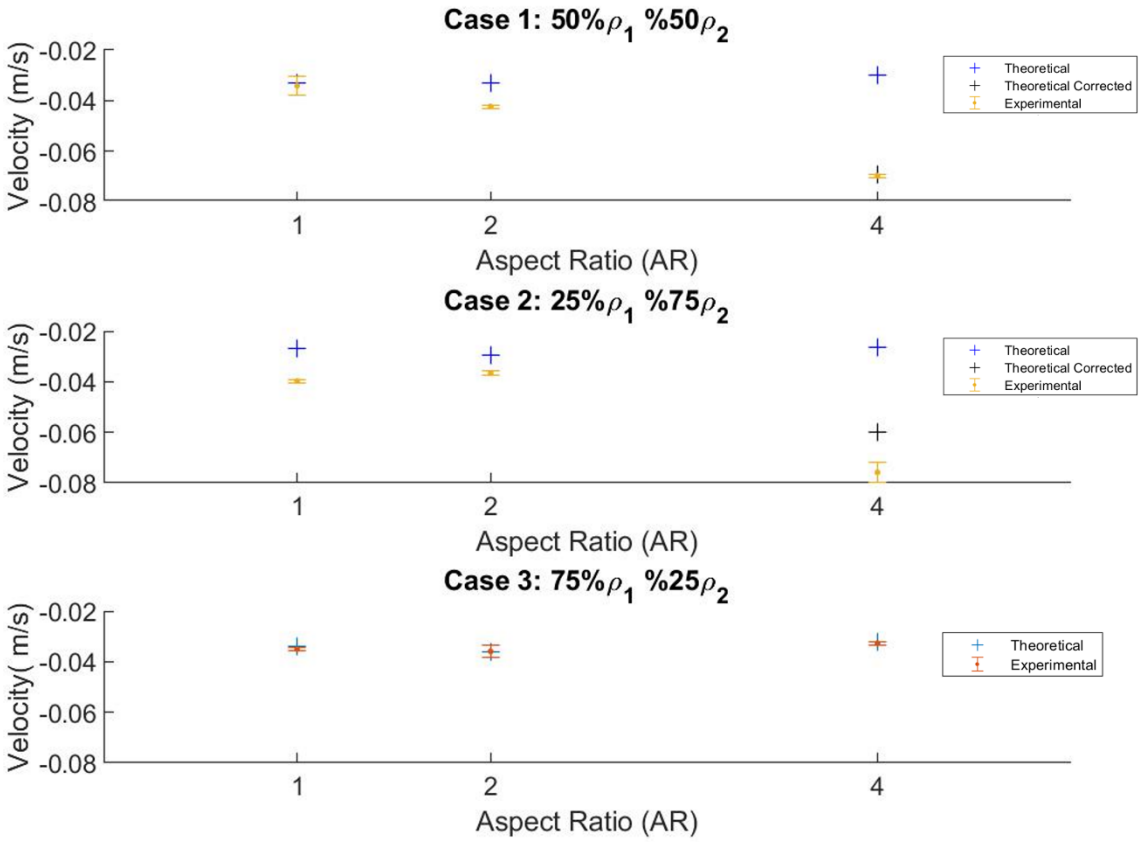

Figure 17. A comparison of predicted and experimental settling velocities of CD cylinders with varying AR. Predicted settling velocities are calculated as described in section 2.1. Errorbars indicate the standard error of mean measurements. Errorbars are calculated by dividing the standard deviation by the square root of the number of measurements of the mean.

For Cases 1 and 2, the experimental velocity was nearly double the predicted (theoretical) velocity. Cylinders were dropped in an initially horizontal orientation. Previous work found that CD cylinders displayed two distinct settling orientations/behaviors: 1) they fell with a constant slanted orientation, with the denser side pointing down, or 2) they fell in periodic oscillation about a vertical orientation, with the denser side down. For these two cases, cylinders of AR = 4 fell in a vertical orientation, with PETG, the denser material, falling first. Due to this vertical, non-periodic falling behavior, the force of drag is significantly reduced relative to the theoretical prediction—the cross-sectional area is much smaller than the predicted falling orientation, allowing for the cylinder to fall at higher terminal velocities. In order to account for the reduced drag observed experimentally, we recalculated the theoretical velocity considering a vertical cylinder orientation. This is a much better predictor of the settling velocity.

Table 4. Case 1 settling velocity results. Average velocity, maximum velocity, and minimum velocity are calculated for each AR.

	AR 1	**AR 2**	**AR 4**
Average Settling Velocity (m/s)	-0.0341	-0.0423	-0.0697
Maximum Settling Velocity (m/s)	-0.0418	-0.0436	-0.0703
Minimum Settling Velocity (m/s)	-0.0303	-0.0416	-0.0691

Table 5. Case 2 settling velocity results. Average velocity, maximum velocity, and minimum velocity are calculated for each AR.

	AR 1	AR 2	AR 4
Average Settling Velocity (m/s)	-0.0397	-0.0366	-0.0759
Maximum Settling Velocity (m/s)	-0.0404	-0.0384	-0.0834
Minimum Settling Velocity (m/s)	-0.0384	-0.0354	-0.0709

Table 6. Case 3 settling velocity results. Average velocity, maximum velocity, and minimum velocity are calculated for each AR.

	AR 1	AR 2	AR 4
Average Settling Velocity (m/s)	-0.0351	-0.0359	-0.0328
Maximum Settling Velocity (m/s)	-0.0359	-0.0410	-0.0341
Minimum Settling Velocity (m/s)	-0.0337	-0.0334	-0.0319

In all density cases, the cylinders showed reasonable repeatability between trials for their measured settling velocity. As mentioned in Chapter 2.1, we predicted that experimental Re will be higher than predicted Re. As defined by equation 1, Re is a function of velocity. When a settling velocity is greater than the predicted value, a recalculation of Re with the true (non-

predicted) value will result in a larger Re. This is largely true for Case 1, with the only disagreement at AR = 1. This variation at AR = 1 is a result of the periodic behavior that occurs at this low AR (as discussed in the next section). As shown in Table 4**,** Case 1 has two trials in which the experimental velocity value is repeated. Again, in Case 2 (Table 5) we see the same experimental velocity achieved twice as well as all cylinders having experimental velocities slightly greater than the predicted velocity value. Case 3 (Table 6) cylinders display the same level of both precision and accuracy as other Cases. This is the only Case where the velocity remained relatively unchanged as AR increases. At AR = 4, these cylinders fell with a constant slanted orientation that was slightly different from the horizontal. This resulted in increased drag, resulting in the cylinder's velocity being (comparatively) independent from AR.

3.3 Cylinder Trajectories

We measured the 3D trajectories and made qualitative observations of cylinder orientation for the nine cases of CD cylinders. Trajectory refers to the path of the cylinder's centroid through 3D space, and orientation refers to the angle that the cylinder's axis of symmetry (AoS) makes with the horizontal. In this study, we tracked the centroid of cylinders in order to have quantitative regarding periodic variation in the lateral coordinate of the tracked cylinders. Cylinders orientation was not tracked, but qualitative results are obtained through observation of high-speed videos of each trial. Previous studies categorized similarly measured trajectories and orientations into three modes:

- Mode 0: cylinders fell with a vertical trajectory and in a horizontal orientation.
- Mode 1: cylinders fell with a slanted trajectory and in a stable, angled orientation.

- Mode 2: cylinders fell with a periodic vertical trajectory, with periodicity about a vertical orientation as they fell.

Mode 0 behavior is typical of UD cylinders and was not observed in any of the CD cylinders considered here. However, because we varied the CoM in new ways, additional trajectories and orientations were observed that do not fit the modes proposed by Angle [10]. Cylinder behavior can be formally grouped into three different modes with more descriptive subcategories:

- Mode 0: cylinders fell with a vertical trajectory and in a horizontal orientation.
- Mode 1: cylinders fell with a slanted trajectory and in a stable, angled orientation.
    - Mode 1.A: cylinders fell at a periodic slanted trajectory, with periodicity about a nearly vertical orientation as they fell.
    - Mode 1.B: cylinders fell at a periodic slanted trajectory, with periodicity about a horizontal orientation as they fell.
- Mode 2: cylinders fell with a periodic vertical trajectory, with periodicity about a vertical orientation as they fell.

Cylinder trajectory is impacted by mass distribution and aspect ratio. Increasing the AR increases the effects of drag and fluid inertia, while varying the mass distribution moves the object's CoM away from its CoB.

In some experimental trials (cylinder drops), the cylinders experience similar trajectories although they do not occur at the same points in space. This is not due to imperfections in the cylinders (as shown by consistency in the terminal velocity values for successful trials) but due to imperfections in the dropping method. The robot claw was intended to increase consistency and remove human error from the dropping process. However, the claw was not submerged in water, so cylinders had to penetrate the free surface prior to being observed by the cameras. This

resulted in a momentary period of free fall through air rather than water, as well as contact with the free surface which may have perturbed the cylinders' initial velocities. This contact may also have made the origin of the cylinders' trajectories inconsistent.

Figure 18 shows the trajectories of Case 1 AR = 1 cylinders all fell with Mode 2 behavior (vertical orientation, vertical trajectory with periodicity) with the PETG (denser) side pointing down. All three trials display similar periodic variation in the lateral coordinates of the tracked cylinders. For cylinders with AR = 2, cylinders continued falling with mode 2 behavior, but amplitude and period of periodic behavior increased.

Cylinders with AR = 4 fell at a slanted trajectory (Mode 1 behavior) experiencing no periodicity. In this trial, the cylinder fell at a constant angle with a slanted trajectory with PETG side pointing down. The cylinder begins falling from the right side (positive y) to left side (negative y) of the tank where it then collides with the wall where it then enters the field of view. The cylinder continued to fall at a constant angle and slanted trajectory until it leaves the cameras FOV. This behavior (slanted trajectory carrying the cylinder out of the field of view) resulted in only one successful trial for AR = 4, and eight unsuccessful trials. During these nine trials, the cylinder qualitatively exhibited the same behavior.

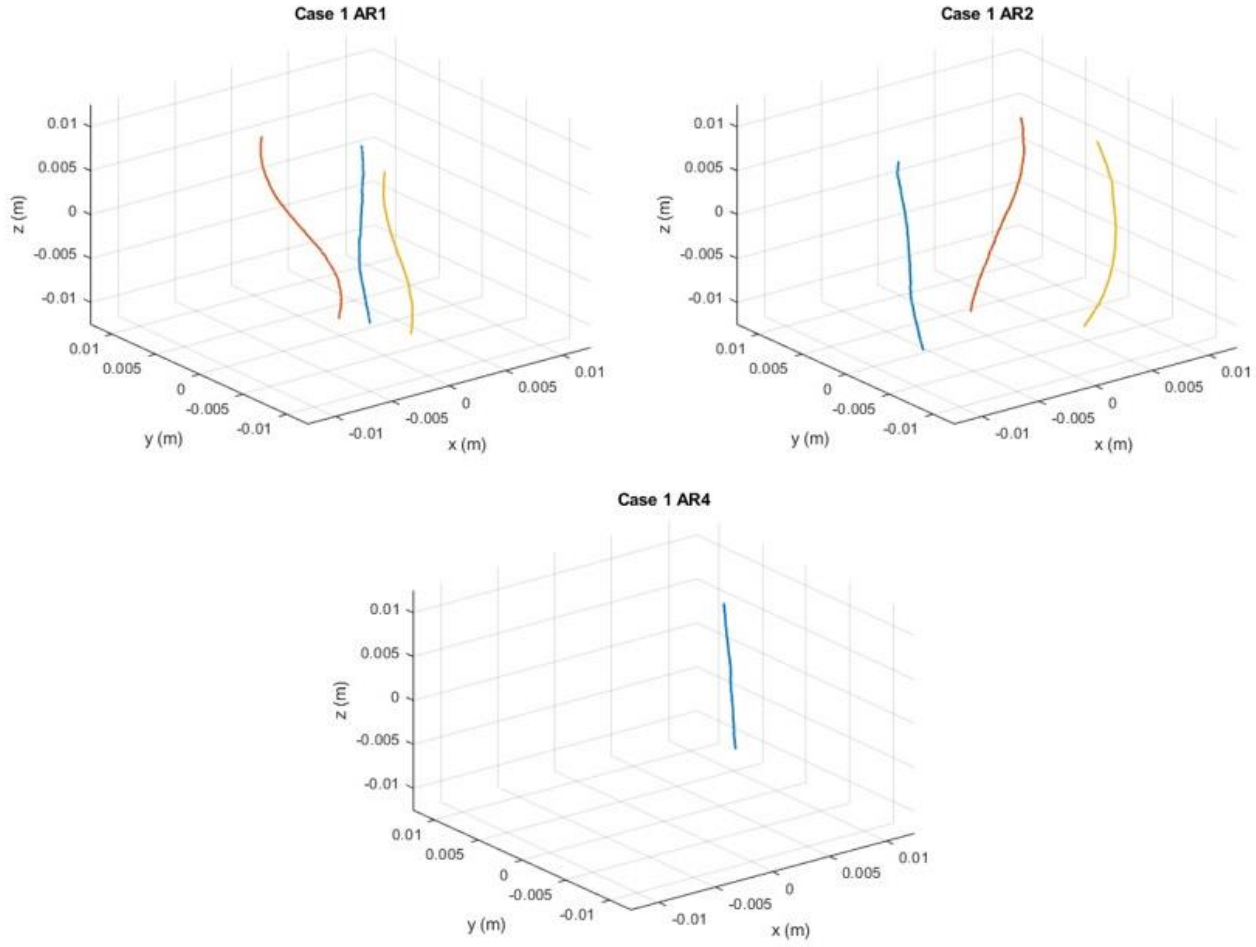

Figure 18. Trajectories of Case 1 cylinders at different AR. Different colors represent different trials.

Case 2 (25% ASA, 75% PETG) (Figure 19) experienced Mode 1 and Mode 1.A behavior; however, this varied depending on the cylinder's aspect ratio. For AR = 1 cylinders, both Mode 1 and Mode 1.A behavior were present. However, AR = 2 cylinders exclusively displayed mode

1.A behavior, with a larger amplitude and period of periodic behavior compared to AR=1 cylinders with the same mass distribution. AR = 4 cylinders solely displayed Mode 1 behavior.

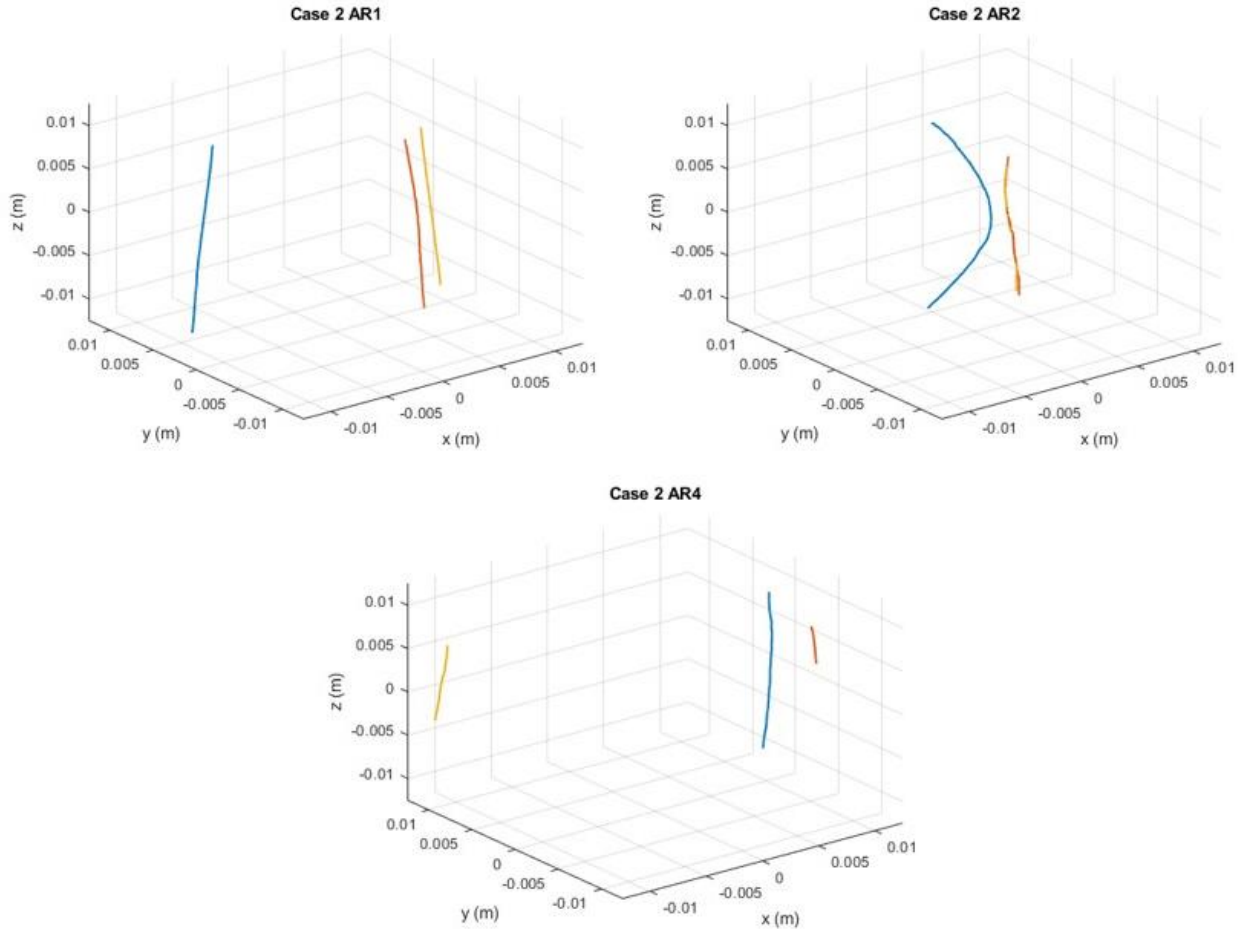

Figure 19. Trajectories of Case 2 cylinders at different AR. Different colors represent different trials.

Case 3 (75% ASA, 25% PETG) (Figure 20) showed Mode 1 and 2 behaviors. AR = 1 cylinders displayed Mode 2 behavior, showing periodic variation in the xy plane with PETG pointing downward, but also experienced rotation about the z axis observed through high-speed videos. The other two Cases did not experience significant motion in the z-direction; most movement (for all three tested aspect ratios) was restricted to the xy plane (all cylinders' initial

orientation was with their principal axis aligned with the x-axis). For AR = 2, cylinders displayed Mode 1, Mode 1.A, and Mode 1.B behavior—all three trials were slightly different. In the first trial of AR = 2, the cylinder fell at a constant slanted angle (Mode 1). In the second trial, the cylinder experienced periodic variation horizontally (Mode 1.B). In the third trial, the cylinder experienced periodic variation vertically (Mode 1A) with PETG pointing down. This led to a less pronounced slant to the trajectory. None of the three different falling behaviors had significant impacts on terminal velocity. Small imperfections in printing may have resulted in the variations in falling behavior, indicating that cylinders with this mass distribution and aspect ratio experience a transitional state (a critical state dependent on CoM, mass distribution, and Re in which the cylinder reaches an equilibrium, resulting in a constant slanted trajectory and orientation). This transitional state also exists at AR = 4, where cylinders showed Mode 1 and Mode 1.A behavior. Again, the difference in falling behavior did not impact the settling velocity for this mass distribution.

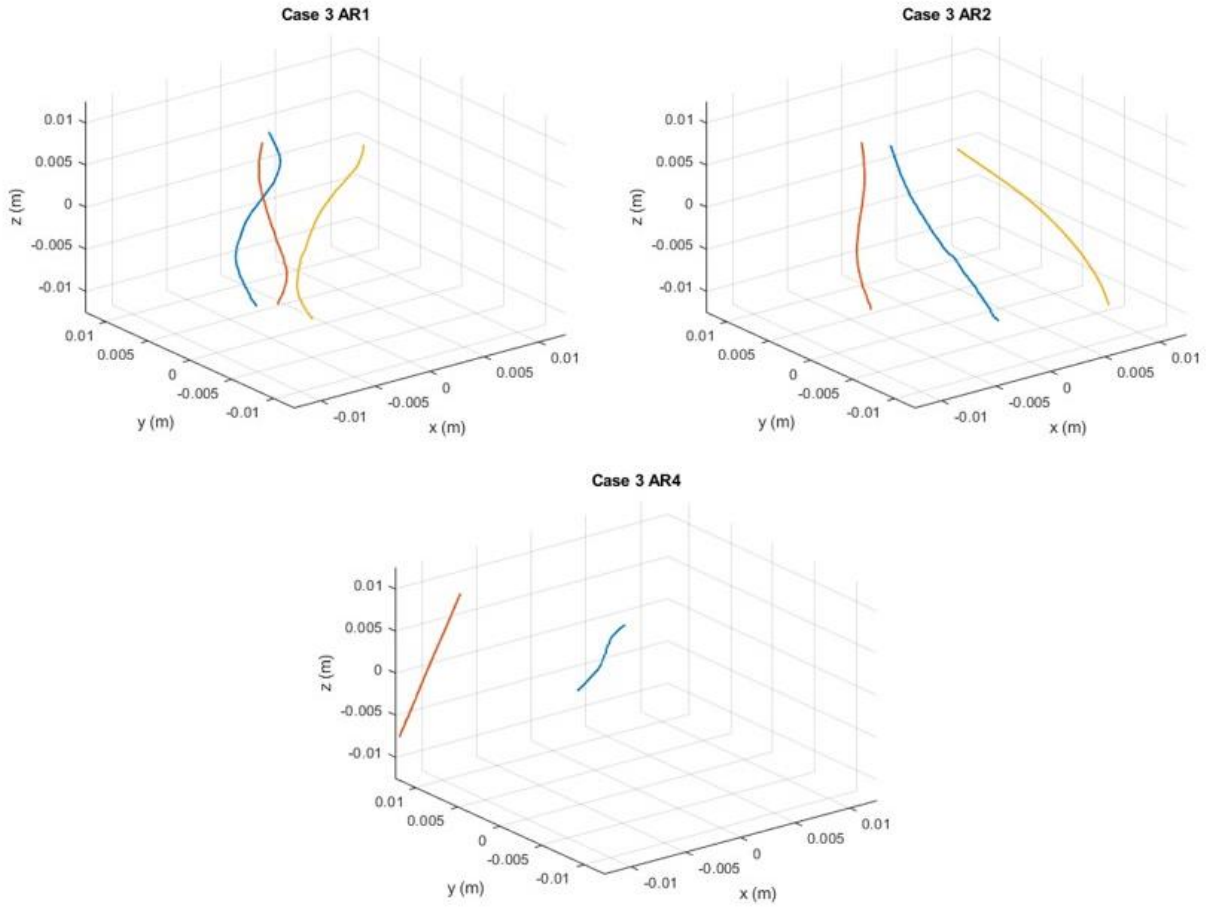

Figure 20. Trajectories of Case 2 cylinders at different AR. Different colors represent different trials.

Chapter 4

Conclusions and Recommendation for Future Work

The primary aim of this study was to validate the use of 3D printing for analyzing the settling behavior of cylindrical particles. Using two high-speed Chronos 1.4 cameras, CD cylinders of AR = 1, 2, and 4 were observed as they fell through water at their terminal velocity. This experiment allowed for image processing using DLTdv8 to track particles in 3D space.

3D printed cylinders successfully demonstrated the three modes of settling behavior as proposed by Angle [10]. By varying the CoM of CD cylinders, additional behaviors were observed, resulting in the following additions to Angle's initial three modes:

- Mode 0: cylinders fell with a vertical trajectory and in a horizontal orientation.
- Mode 1: cylinders fell with a slanted trajectory and in a stable, angled orientation.
    - Mode 1.A: cylinders fell at a periodic slanted trajectory, with periodicity about a nearly vertical orientation as they fell.
    - Mode 1.B: cylinders fell at a periodic slanted trajectory, with periodicity about a horizontal orientation as they fell.
- Mode 2: cylinders fell with a periodic vertical trajectory, with periodicity about a vertical orientation as they fell.

Cylinders at an AR = 1 either experienced Mode 1, Mode 1.A, or Mode 3 behavior. At AR = 2, periodicity increased and all cylinders exhibit Mode 1.A or Mode 1.B behavior. Following Mode 1.B behavior, there exists a transitional state in which the cylinder transitions to Mode 1 behavior. At this mode, cylinders experienced a slanted trajectory with a stable, angled fall orientation. After a cylinder exceeds this transitional state, Mode 2 behavior is achieved.

Given the results from the initial trials in this study, there is a clear relationship between AR and mass distribution on cylinders settling behaviors. It is hypothesized that there is a transitional regime at AR = 2 and AR = 4 where cylinders reach an equilibrium Mode 1 behavior. However, this Mode 1 behavior is a function of mass distribution as well as AR and Re. Future work may benefit from an increased FOV allowing for more experimental videos at these transitional AR and mass distribution cases to be recorded in every drop situation. In order to provide greater consistency, the design and inclusion of a new base allowing the robot claw to be submerged in the tank will provide increased consistency in particle drops. Submerging the robot claw removes variation in how particles impact the free surface, resulting in more consistent trajectories in the FOV. With a more robust dropping system and larger FOV, obtaining a larger sample of data will allow more concrete connections to AR and mass distribution to be drawn.

Future work may benefit from a density analysis of a large sample of 3D printed cylinders. In this study, 3D printed cylinders provided consistent and repeatable results. Validating that the density of 3D printed particles is also needed. This will ensure that 3D printed cylinders are at the targeted densities and Re.

Lastly, including well defined markers on each cylinder will allow for more robust particle tracking. With a clear marker at the centroid and on each end on the cylinder, quantitative analysis on cylinder orientation will allow for conclusions about particle orientations. The addition of this computational work combined with laboratory experiments will aid in the understanding of nonspherical particles with nonuniform mass densities in nature. This understanding will in turn lead to a fuller conception of important processes such as natural

sedimentation of marine snow aggregates and the transport of particulate pollutants such as microplastics.

Appendix A

Cylinder Fabrication Code

```
clc;
clear all;
close all;

nu = 1.12E-6; % [m^2/s] Kinematic viscosity of fluid
rho_f = 1000; % [kg/m^3] Density of fluid
D1=1027;      % [kg/m^3] Density of PLA
D2=1007;      % [kg/m^3] Density of ASA
% rho_p = .5*D1+.5*D2; % [kg/m^3] 50% D1 50% D2
rho_p = .25*D1+.75*D2; % [kg/m^3] 25% D1 75% D2
% rho_p = .75*D1+.25*D2; % [kg/m^3] 75% D1 25% D2
SG = rho_p./rho_f;

d_p = 4.8; % diameter of the cylinder
l_p = d_p*4; % length of the cylinder
AR = l_p./d_p; % Aspect Ratio of cylinder (in paper E)

%% Ellipsoid fit
a = d_p/2; % Semi-minor axis 1
b = a; % Semi-minor axis 2
c = l_p/2; % Semi-minor axis 3

V = pi*a.*b.*c.*2; % Volume of the ellipsoid fit
r_eqV = (V*0.75./pi).^(1/3); % Radius of the sphere with equiv.
volume

SA = 2*pi.*a.*l_p + 2*pi.*a.* b; % Surface area of the ellipsoid
r_eqSA = (SA/(4*pi)).^0.5; % Radius of sphere with equiv.
surface area

d = 2*a.*(3*AR/2).^(1/3);  % Equivalent volume diameter ; Eq.19

%%
A_s = (2*AR + 1)./((18*AR.^2)).^(1/3); % Eq. 19 ; Normalized
A_surf = (SA./(pi*4*r_eqV.^2)); % Normalized surface area w.r.t
sphere
A_s1 = A_surf - 1; % Excess surface area factor; refer eq. 25
A_pr1 = (2*a.*l_p)./(pi*d.^2/4); % Projected area
A_pr2 = (2*b.*l_p)./(pi*d.^2/4);
```

```
A_pr3 = (pi*a.*b)./(pi*d.^2/4);

if AR >= 1        % Eq 25 & 26
    C_shape = 1 + 0.7*sqrt(A_s1) + 2.4*A_s1;
else
    C_shape = 1 + 1.5*sqrt(A_s1) + 6.7*A_s1;
end

if AR <= 1        % Eq. 16
    f_shape = ((AR.^(-1/3)).*sqrt(1-AR.^2))./(acos(AR));
else
    f_shape = ((AR.^(-1/3)).*sqrt(AR.^2 - 1))./log(AR +
sqrt(AR.^2 - 1));
end

fg_fb = 9.81*V.*(1E-9).*(SG-1).*rho_f;
U = .037; % Clift-Gauvin iterative. Change this value until
fg_fb=fd. THIS IS A GUESS!

Re = (U.*2*r_eqV./1000)./nu;
Re_c = C_shape.*Re./f_shape; % Normalized Reynolds number Eq. 28

C_D_c = ((24/Re_c).*(1 + 0.15.*(Re_c.^0.687))) + (0.42./(1 +
(42500./(Re_c.^1.16)))); % Eq. 8
C_D = C_D_c.*C_shape; % Normalized Eq. 28


FD = 5E-7*(rho_f.*C_D.*pi.*r_eqSA.^2.*U.^2); % Drag force

iteration = fg_fb-FD;
i=0;
for i=0:1000000;
if iteration > 2.954418276544490e-08;
    U = U+.0001;
    Re = (U.*2*r_eqV./1000)./nu;
    Re_c = C_shape.*Re./f_shape; % Normalized Reynolds number
Eq. 28

    C_D_c = ((24/Re_c).*(1 + 0.15.*(Re_c.^0.687))) + (0.42./(1 +
(42500./(Re_c.^1.16)))); % Eq. 8
    C_D = C_D_c.*C_shape; % Normalized Eq. 28

    FD = 5E-7*(rho_f.*C_D.*pi.*r_eqSA.^2.*U.^2); % Drag force
    iteration = fg_fb-FD;
elseif iteration < -2.954418276544490e-08;
    U = U-.0001;
```

```
    Re = (U.*2*r_eqV./1000)./nu;
    Re_c = C_shape.*Re./f_shape; % Normalized Reynolds number
Eq. 28

    C_D_c = ((24/Re_c).*(1 + 0.15.*(Re_c.^0.687))) + (0.42./(1 +
(42500./(Re_c.^1.16)))); % Eq. 8
    C_D = C_D_c.*C_shape; % Normalized Eq. 28


    FD = 5E-7*(rho_f.*C_D.*pi.*r_eqSA.^2.*U.^2); % Drag force
    iteration = fg_fb-FD;
end
end


fprintf('The dimensions of the cylinder are
a=%1.2fmm,b=%1.2fmm,c=%1.2fmm\n', a,b,c);
fprintf('The predicted Reynolds Number is %1.2f\n', Re)
fprintf('The predicted Velocity is %1.4f\n', U)
```

Converting MP4 Videos to MATLAB Array

```
% This code reads the video and saves each frame in a array to
be read by further processing codes.

clear; clc;

v = VideoReader('cam2.mp4'); % VideoReader loads the video to
the workspace of MATLAB.
N = v.NumFrames; % N is the number of frames in video "v".

% In case you are using MATLAB 2018b or older. Using
"NumberofFrames" creates
% a conflict with "hasFrame", that's way you should overwrtite
"N" by imput
% the number of frames manually after getting the number from
% "NumberofFrames".
% N = v.NumberOfFrames;
% N = 3047;

%%
% Next we will create the array(Frames), that contains the
frames from the video.

% RangeFrame is a vector containing the frames that you are
% interested in analyze. For this case it selects every
thirtieth frame,
% starting with frame one and ending at half the video "v".
RangeFrame = 1:30:round(N);
n = length(RangeFrame); % n is the final number of frames in the
array.

e = 1;
CurFrame = 0;
tic;
while hasFrame(v)       % This while loop will go from frame one
to frame N of "v".
    fprintf('Processing %d of %d ...',e,n);
    CurImage = readFrame(v); % This is the current image of the
video, again it goes from one to frame N of "v".
    CurFrame = CurFrame+1; % This count specifies the current
frame that has been read in "CurImage".
    % Here we check if "CurFrame" is part of "RangeFrame" and if
it is positive we proced to save it in the array "Frames".
    if ismember(CurFrame,RangeFrame)
```

```
        % By modifying the rows and columns of "CurImage", you
can cut the
        % video. In this case we reduce the original (1024x1024
px), to one
        % of size 100x530 px. The area where the action happens.
        Frames(:,:,e) = CurImage(1:1024,1:1024);
        e = e+1;
    end
    clc;
    % Since we are interested in only half of the original
video, we should
    % stop the while loop when we reach this point.
    if e > n
        break
    end
end
toc;
%%
% In case you need visual inspection of the final sequence,
before saving.
for e =1:n
    imshow(Frames(:,:,e))
end

%%
% Saving the array for further manipulation.
fprintf('Saving Frames into .mat file')
save('cam2.mat','Frames','-v7.3')
clc;
fprintf('Array created')
```

Calibration

```
clc, clear

% check for the right MATLAB toolbox
if exist('detectCheckerboardPoints')~=2
  disp('Sorry, you need the detectCheckerboardPoints function
from the CoMputer Vision toolbox to run this script')
  return
end
expectedSize=54;
load('cam1.mat')
[Ypx Xpx NoFrames]=size(Frames);
% process camera 1
c1data={};
for i=1:NoFrames
 Im = Frames(:,:,i);
 I=detectCheckerboardPoints(Frames(:,:,i));
         if size(I,1)==expectedSize
              c1data{i,1}=I;
         else
              c1data{i,1}=NaN(54,2);
         end

end
clear Im Frames I i
% process camera 2
load('cam2.mat')
[Ypx Xpx NoFrames]=size(Frames);

c2data={};
for i=1:NoFrames
 Im = Frames(:,:,i);
 I=detectCheckerboardPoints(Frames(:,:,i));
         if size(I,1)==expectedSize
              c2data{i,1}=I;
         else
              c2data{i,1}=NaN(54,2);
         end

end

% let's build a wand - an array of paired points that should
have a constant
% length regardless of their position in the calibrated volume
```

```
wand=[];
for i=1:NoFrames

wand=[wand;[c1data{i}(1,:),c2data{i}(1,:),c1data{i}(end,:),c2dat
a{i}(end,:)]];
end

bkg=[cat(1,c1data{:}),cat(1,c2data{:})];

dlmwrite('bkg.csv',bkg)
dlmwrite('wand.csv',wand);
```

Analysis Code

```
%% Plotting Velocity
AR = [1 2 4];

Case1_theo = [-.0331 -.0331 -.0299];
Case1_theo_2 = [NaN NaN, -.0691];
Case1_exp_1 = [-.0303 -.0418 -.0703];
Case1_exp_2 = [-.0303 -.0436 NaN];
Case1_exp_3 = [-.0418 -.0416 NaN];
Case1 = [-.03413 -.04233 -.0697];
err1 = [.00383 .00064 .0006];

Case2_theo = [-.0267 -.0295 -.0265];
Case2_theo_2 = [NaN NaN, -.0601];
Case2_exp_1 = [-.0404 -.0354 -.0733];
Case2_exp_2 = [-.0404 -.0384 -.0709];
Case2_exp_3 = [-.0384  -.0361 -.0834];
Case2 = [-.03973 -.03663 -.07587];
err2 = [.00067 .00091 .00383];

Case3_theo = [-.0338 -.0360 -.0323];
Case3_exp_1 = [-.0359 -.0334 -.0341];
Case3_exp_2 = [-.0356 -.0334 -.0319];
Case3_exp_3 = [-.0337 -.0410 NaN];
Case3 = [-.03507 -.03593 -.03277];
err3 = [.00069 .00253 .00068];

figure(1)
subplot(3,1,1)
scatter(AR,Case1_theo,'+','b')
hold on
scatter(AR,Case1_theo_2,'+','k')
errorbar(AR,Case1,err1,'.')

xticks([1 2 4])
xlim([0 5])
ylim([-.08,-.02])
title('Case 1: 50%\rho_1 %50\rho_2')
xlabel('Aspect Ratio (AR)')
ylabel('Velocity (m/s)')
legend('Theoretical','Theoretical
Corrected','Experimental','Location','northeast')

subplot(3,1,2)
```

```
scatter(AR,Case2_theo,'+','b')
hold on
scatter(AR,Case2_theo_2,'+','k')
errorbar(AR,Case2,err2,'.')

xticks([1 2 4])
xlim([0 5])
ylim([-.08,-.02])
title('Case 2: 25%\rho_1 %75\rho_2')
xlabel('Aspect Ratio (AR)')
ylabel('Velocity (m/s)')

legend('Theoretical','Theoretical
Corrected','Experimental','Location','northeast')

subplot(3,1,3)
scatter(AR,Case3_theo,'+')
hold on
errorbar(AR,Case3,err3,'.')

xticks([1 2 4])
xlim([0 5])
ylim([-.08,-.02])
title('Case 3: 75%\rho_1 %25\rho_2')
xlabel('Aspect Ratio (AR)')
ylabel('Velocity( m/s)')
legend('Theoretical','Experimental','Location','northeast')

%% Plotting Position Case 1
%AR1
a1=readtable('Case1_AR1xyzpts.csv');
a1( any(ismissing(a1),2), :) = [];
y1=table2array(a1(:,2));
x1=table2array(a1(:,1));
z1=table2array(a1(:,3));

a2=readtable('Case1_AR1_2xyzpts.csv');
a2( any(ismissing(a2),2), :) = [];
y2=table2array(a2(:,2));
x2=table2array(a2(:,1));
z2=table2array(a2(:,3));

a3=readtable('Case1_AR1_3xyzpts.csv');
a3( any(ismissing(a3),2), :) = [];
y3=table2array(a3(:,2));
x3=table2array(a3(:,1));
```

```
z3=table2array(a3(:,3));

figure
subplot(3,1,1)
plot3(z1,x1,y1,'LineWidth',1.5)
grid on
hold on
plot3(z2,x2,y2,'LineWidth',1.5)
plot3(z3,x3,y3,'LineWidth',1.5)
title('Case 1 AR1')
zlabel('z (m)')
ylabel('y (m)')
xlabel('x (m)')
zlim([-1.25E-2,1.25E-2])
ylim([-1.25E-2,1.25E-2])
xlim([-1.25E-2,1.25E-2])
zticks([-1E-2 -.5E-2  0 .5E-2 1E-2])
xticks([-1E-2 -.5E-2  0 .5E-2 1E-2])
yticks([-1E-2 -.5E-2  0 .5E-2 1E-2])


%AR2
a1=readtable('Case1_AR2xyzpts.csv');
a1( any(ismissing(a1),2), :) = [];
y1=table2array(a1(:,2));
x1=table2array(a1(:,1));
z1=table2array(a1(:,3));

a2=readtable('Case1_AR2_2xyzpts.csv');
a2( any(ismissing(a2),2), :) = [];
y2=table2array(a2(:,2));
x2=table2array(a2(:,1));
z2=table2array(a2(:,3));

a3=readtable('Case1_AR2_3xyzpts.csv');
a3( any(ismissing(a3),2), :) = [];
y3=table2array(a3(:,2));
x3=table2array(a3(:,1));
z3=table2array(a3(:,3));

subplot(3,1,2)
plot3(z1,y1,x1,'LineWidth',1.5)
grid on
hold on
plot3(z2,y2,x2,'LineWidth',1.5)
plot3(z3,y3,x3,'LineWidth',1.5)
```

```
title('AR2')
zlabel('z (m)')
ylabel('y (m)')
xlabel('x (m)')
zlim([-1.25E-2,1.25E-2])
ylim([-1.25E-2,1.25E-2])
xlim([-1.25E-2,1.25E-2])
zticks([-1E-2 -.5E-2  0 .5E-2 1E-2])
xticks([-1E-2 -.5E-2  0 .5E-2 1E-2])
yticks([-1E-2 -.5E-2  0 .5E-2 1E-2])

%AR4
a1=readtable('Case1_AR4xyzpts.csv');
a1( any(ismissing(a1),2), :) = [];
y1=table2array(a1(:,2));
x1=table2array(a1(:,1));
z1=table2array(a1(:,3));

% a2=readtable('Case1_AR4_2xyzpts.csv');
% a2( any(ismissing(a2),2), :) = [];
% y2=table2array(a2(:,2));
% x2=table2array(a2(:,1));

% a3=readtable('Case1_AR4_3xyzpts.csv');
% a3( any(ismissing(a2),2), :) = [];
% y3=table2array(a2(:,2));
% x3=table2array(a2(:,1));


subplot(3,1,3)
plot3(z1,y1,x1,'LineWidth',1.5)
grid on
hold on
%plot(x2,y2,z2)
%plot(x3,y3,z3)
title('AR4')
zlabel('z (m)')
ylabel('y (m)')
xlabel('x (m)')
zlim([-1.25E-2,1.25E-2])
ylim([-1.25E-2,1.25E-2])
xlim([-1.25E-2,1.25E-2])
zticks([-1E-2 -.5E-2  0 .5E-2 1E-2])
xticks([-1E-2 -.5E-2  0 .5E-2 1E-2])
yticks([-1E-2 -.5E-2  0 .5E-2 1E-2])
```

```
%% Plotting Position Case 2
%AR1
a1=readtable('Case2_AR1xyzpts.csv');
a1( any(ismissing(a1),2), :) = [];
y1=table2array(a1(:,2));
x1=table2array(a1(:,1));
z1=table2array(a1(:,3));

a2=readtable('Case2_AR1_2xyzpts.csv');
a2( any(ismissing(a2),2), :) = [];
y2=table2array(a2(:,2));
x2=table2array(a2(:,1));
z2=table2array(a2(:,3));

a3=readtable('Case2_AR1_3xyzpts.csv');
a3( any(ismissing(a3),2), :) = [];
y3=table2array(a3(:,2));
x3=table2array(a3(:,1));
z3=table2array(a3(:,3));

figure
subplot(3,1,1)
plot3(z1,y1,x1,'LineWidth',1.5)
grid on
hold on
plot3(z2,y2,x2,'LineWidth',1.5)
plot3(z3,y3,x3,'LineWidth',1.5)
title('Case 2 AR1')
zlabel('z (m)')
ylabel('y (m)')
xlabel('x (m)')
zlim([-1.25E-2,1.25E-2])
ylim([-1.25E-2,1.25E-2])
xlim([-1.25E-2,1.25E-2])
zticks([-1E-2 -.5E-2  0 .5E-2 1E-2])
xticks([-1E-2 -.5E-2  0 .5E-2 1E-2])
yticks([-1E-2 -.5E-2  0 .5E-2 1E-2])

%AR2
a1=readtable('Case2_AR2xyzpts.csv');
a1( any(ismissing(a1),2), :) = [];
y1=table2array(a1(:,2));
x1=table2array(a1(:,1));
z1=table2array(a1(:,3));

a2=readtable('Case2_AR2_2xyzpts.csv');
```

```
a2( any(ismissing(a2),2), :) = [];
y2=table2array(a2(:,2));
x2=table2array(a2(:,1));
z2=table2array(a2(:,3));

a3=readtable('Case2_AR2_3xyzpts.csv');
a3( any(ismissing(a3),2), :) = [];
y3=table2array(a3(:,2));
x3=table2array(a3(:,1));
z3=table2array(a3(:,3));

subplot(3,1,2)
plot3(z1,y1,x1,'LineWidth',1.5)
hold on
grid on
plot3(z2,y2,x2,'LineWidth',1.5)
plot3(z3,y3,x3,'LineWidth',1.5)
title('AR2')
zlabel('z (m)')
ylabel('y (m)')
xlabel('x (m)')
zlim([-1.25E-2,1.25E-2])
ylim([-1.25E-2,1.25E-2])
xlim([-1.25E-2,1.25E-2])
zticks([-1E-2 -.5E-2  0 .5E-2 1E-2])
xticks([-1E-2 -.5E-2  0 .5E-2 1E-2])
yticks([-1E-2 -.5E-2  0 .5E-2 1E-2])

%AR4
a1=readtable('Case2_AR4xyzpts.csv');
a1( any(ismissing(a1),2), :) = [];
y1=table2array(a1(:,2));
x1=table2array(a1(:,1));
z1=table2array(a1(:,3));

a2=readtable('Case2_AR4_2xyzpts.csv');
a2( any(ismissing(a2),2), :) = [];
y2=table2array(a2(:,2));
x2=table2array(a2(:,1));
z2=table2array(a2(:,3));

a3=readtable('Case2_AR4_3xyzpts.csv');
a3( any(ismissing(a3),2), :) = [];
y3=table2array(a3(:,2));
x3=table2array(a3(:,1));
z3=table2array(a3(:,3));
```

```
subplot(3,1,3)
plot3(z1,y1,x1,'LineWidth',1.5)
hold on
grid on
plot3(z2,y2,x2,'LineWidth',1.5)
plot3(z3,y3,x3,'LineWidth',1.5)
title('AR4')
zlabel('z (m)')
ylabel('y (m)')
xlabel('x (m)')
zlim([-1.25E-2,1.25E-2])
ylim([-1.25E-2,1.25E-2])
xlim([-1.25E-2,1.25E-2])
zticks([-1E-2 -.5E-2  0 .5E-2 1E-2])
xticks([-1E-2 -.5E-2  0 .5E-2 1E-2])
yticks([-1E-2 -.5E-2  0 .5E-2 1E-2])

%% Position Case 3
%AR1
a1=readtable('Case3_AR1xyzpts.csv');
a1( any(ismissing(a1),2), :) = [];
y1=table2array(a1(:,2));
x1=table2array(a1(:,1));
z1=table2array(a1(:,3));

a2=readtable('Case3_AR1_2xyzpts.csv');
a2( any(ismissing(a2),2), :) = [];
y2=table2array(a2(:,2));
x2=table2array(a2(:,1));
z2=table2array(a2(:,3));

a3=readtable('Case3_AR1_3xyzpts.csv');
a3( any(ismissing(a3),2), :) = [];
y3=table2array(a3(:,2));
x3=table2array(a3(:,1));
z3=table2array(a3(:,3));

figure
subplot(3,1,1)
plot3(z1,y1,x1,'LineWidth',1.5)
hold on
grid on
plot3(z2,y2,x2,'LineWidth',1.5)
plot3(z3,y3,x3,'LineWidth',1.5)
```

```
title('Case 3 AR1')
zlabel('z (m)')
ylabel('y (m)')
xlabel('x (m)')
zlim([-1.25E-2,1.25E-2])
ylim([-1.25E-2,1.25E-2])
xlim([-1.25E-2,1.25E-2])
zticks([-1E-2 -.5E-2  0 .5E-2 1E-2])
xticks([-1E-2 -.5E-2  0 .5E-2 1E-2])
yticks([-1E-2 -.5E-2  0 .5E-2 1E-2])

%AR2
a1=readtable('Case3_AR2xyzpts.csv');
a1( any(ismissing(a1),2), :) = [];
y1=table2array(a1(:,2));
x1=table2array(a1(:,1));
z1=table2array(a1(:,3));

a2=readtable('Case3_AR2_2xyzpts.csv');
a2( any(ismissing(a2),2), :) = [];
y2=table2array(a2(:,2));
x2=table2array(a2(:,1));
z2=table2array(a2(:,3));

a3=readtable('Case3_AR2_3xyzpts.csv');
a3( any(ismissing(a3),2), :) = [];
y3=table2array(a3(:,2));
x3=table2array(a3(:,1));
z3=table2array(a3(:,3));

subplot(3,1,2)
plot3(z1,y1,x1,'LineWidth',1.5)
hold on
grid on
plot3(z2,y2,x2,'LineWidth',1.5)
plot3(z3,y3,x3,'LineWidth',1.5)
title('AR2')
zlabel('z (m)')
ylabel('y (m)')
xlabel('x (m)')
zlim([-1.25E-2,1.25E-2])
ylim([-1.25E-2,1.25E-2])
xlim([-1.25E-2,1.25E-2])
zticks([-1E-2 -.5E-2  0 .5E-2 1E-2])
xticks([-1E-2 -.5E-2  0 .5E-2 1E-2])
yticks([-1E-2 -.5E-2  0 .5E-2 1E-2])
```

```
%AR4
a1=readtable('Case3_AR4xyzpts.csv');
a1( any(ismissing(a1),2), :) = [];
y1=table2array(a1(:,2));
x1=table2array(a1(:,1));
z1=table2array(a1(:,3));

a2=readtable('Case3_AR4_2xyzpts.csv');
a2( any(ismissing(a2),2), :) = [];
y2=table2array(a2(:,2));
x2=table2array(a2(:,1));
z2=table2array(a2(:,3));


subplot(3,1,3)
plot3(z1,y1,x1,'LineWidth',1.5)
hold on
grid on
plot3(z2,y2,x2,'LineWidth',1.5)
title('AR4')
zlabel('z (m)')
ylabel('y (m)')
xlabel('x (m)')
zlim([-1.25E-2,1.25E-2])
ylim([-1.25E-2,1.25E-2])
xlim([-1.25E-2,1.25E-2])
zticks([-1E-2 -.5E-2  0 .5E-2 1E-2])
xticks([-1E-2 -.5E-2  0 .5E-2 1E-2])
yticks([-1E-2 -.5E-2  0 .5E-2 1E-2])
```

BIBLIOGRAPHY

[1] L. T. Bach, T. Boxhammer, A. Larsen, N. Hildebrandt, K. G. Schulz, and U. Riebesell, "Influence of plankton community structure on the sinking velocity of marine aggregates," *Global Biogeochemical Cycles*, vol. 30, no. 8, pp. 1145–1165, Aug. 2016, doi: 10.1002/2016GB005372.

[2] A. Gärdes, M. H. Iversen, H. P. Grossart, U. Passow, and M. S. Ullrich, "Diatom-associated bacteria are required for aggregation of Thalassiosira weissflogii," *ISME Journal*, vol. 5, no. 3, pp. 436–445, Mar. 2011, doi: 10.1038/ismej.2010.145.

[3] A. L. Alldredge, U. Passow, and B. E. Logan, "The abundance and significance of a class of large, transparent organic particles in the ocean," *Deep Sea Research Part I: Oceanographic Research Papers*, vol. 40, no. 6, pp. 1131–1140, Jun. 1993, doi: 10.1016/0967-0637(93)90129-Q.

[4] Y. Li, H. Zhang, and C. Tang, "A review of possible pathways of marine microplastics transport in the ocean," *Anthropocene Coasts*, vol. 3, no. 1, pp. 6–13, 2020, doi: 10.1139/anc-2018-0030.

[5] C. M. Turley and K. Lochte, "Microbial response to the input of fresh detritus to the deep-sea bed," *Global and Planetary Change*, vol. 3, no. 1, pp. 3–23, 1990, doi: 10.1016/0921-8181(90)90052-E.

[6] S. Meng and Y. Liu, "New insights into transparent exopolymer particles (TEP) formation from precursor materials at various Na + /Ca 2+ ratios," *Scientific Reports*, vol. 6, Jan. 2016, doi: 10.1038/srep19747.

[7] A. Engel and M. Schartau, “Influence of transparent exopolymer particles (TEP) on sinking velocity of Nitzschia closterium aggregates,” *Marine Ecology Progress Series*, vol. 182, pp. 69–76, 1999, doi: 10.3354/meps182069.

[8] A. S. Ogston and R. W. Sternberg, “Sediment-transport events on the northern California continental shelf,” *Marine Geology*, vol. 154, no. 1, pp. 69–82, 1999, doi: 10.1016/S0025-3227(98)00104-2.

[9] S. Yasseri, “Experiment of free-falling cylinders in water,” *Underwater Technology*, vol. 32, no. 3, pp. 177–191, Nov. 2014, doi: 10.3723/ut.32.177.

[10] B. Angle, “Density Distribution Effects on the Settling Dynamics of Nonspherical Intertial Particles at Intermediate Reynolds Numbers,” *Proceedings of the ASME-JSME-KSME 2019 8th Joint Fluids Engineering Conference.* , vol. 5, 2019, doi: 10.1115/AJKFluids2019-5458.

[11] R. E. Khayat and R. G. Cox, “Inertia effects on the motion of long slender bodies,” *Journal of Fluid Mechanics*, vol. 209, pp. 435–462, 1989, doi: 10.1017/S0022112089003174.

[12] F. Candelier and B. Mehlig, “Settling of an asymmetric dumbbell in a quiescent fluid,” *Journal of Fluid Mechanics*, vol. 802, pp. 174–185, Sep. 2016, doi: 10.1017/jfm.2016.350.

[13] A. Roy, R. J. Hamati, L. Tierney, D. L. Koch, and G. A. Voth, “Inertial torques and a symmetry breaking orientational transition in the sedimentation of slender fibres,” *Journal of Fluid Mechanics*, vol. 875, pp. 576–596, Sep. 2019, doi: 10.1017/jfm.2019.492.

[14] E. Loth, “Drag of non-spherical solid particles of regular and irregular shape,” *Powder Technology*, vol. 182, no. 3, pp. 342–353, Mar. 2008, doi: 10.1016/j.powtec.2007.06.001.

[15] R. Clift and W. H. Gauvin’, “Motion of Entrained Particles in Gas Streams,” *Can. J. Chem. Eng.*, pp. 439–448, 1971, doi: 10.1002/cjce.5450490403.

[16] G. Bagheri and C. Bonadonna, “On the drag of freely falling non-spherical particles,” *Powder Technology*, vol. 301, pp. 526–544, Nov. 2016, doi: 10.1016/j.powtec.2016.06.015.

[17] Formlabs, “Form 3+,” 2022. https://formlabs.com/3d-printers/form-3/ (accessed Feb. 04, 2022).

[18] H. Yang *et al.*, “Performance evaluation of ProJet multi-material jetting 3D printer,” *Virtual and Physical Prototyping*, vol. 12, no. 1, pp. 95–103, Jan. 2017, doi: 10.1080/17452759.2016.1242915.

[19] A. A. Chaudhari, A. M. Godase, J. Ravindra, and N. Abhijit, “Acetone Vapor Smoothing: A Postprocessing Method for 3D Printed ABS Parts,” *International Journal of Research and Scientific Innovation (IJRSI)* |, vol. 4, no. 5, pp. 123–127, 2017.

[20] R. H. Magarvey and R. L. Bishop, “TRANSITION RANGES FOR THREE-DIMENSIONAL WAKES’,” *Canadian Journal of Physics*, vol. 39, pp. 1418–1422, 1961.

[21] C. Johnson, X. Li, and B. Logan, “Settling Velocities of Fractal Aggregates,” *Environ. Sci. Technol.*, vol. 30, no. 6, pp. 1911–1918, 1996, doi: 10.1021/es950604g.

[22] G. G. Zilliac, D. Degani, and M. Tobak, “Asymmetric vortices on a slender body of revolution,” *AIAA Journal*, vol. 29, no. 5, pp. 667–675, 1991, doi: 10.2514/3.59934.

[23] D. H. Theriault *et al.*, “A protocol and calibration method for accurate multi-camera field videography,” *Journal of Experimental Biology*, vol. 217, no. 11, pp. 1843–1848, Jun. 2014, doi: 10.1242/jeb.100529.

[24] Y. I. Abdel-Aziz and H. M. Karara, “Direct linear transformation from comparator coordinates into object space coordinates in close-range photogrammetry,” *Photogrammetric Engineering and Remote Sensing*, vol. 81, no. 2, pp. 103–107, 2015, doi: 10.14358/PERS.81.2.103.

[25] T. L. Hedrick, “Software techniques for two- and three-dimensional kinematic measurements of biological and biomimetic systems,” *Bioinspiration and Biomimetics*, vol. 3, no. 3, Sep. 2008, doi: 10.1088/1748-3182/3/3/034001.

ACADEMIC VITA

EDUCATION

The Pennsylvania State University University Park, PA
College of Engineering May 2022
Bachelor of Science in Mechanical Engineering
Schreyer Honors College

EXPERIENCE

First Level Inc York, PA
Microelectronics Engineering Intern May 2021 – Current

- Developed and evaluated processes for production of microelectronic packages including wafer dicing, die attach, wire bond, encapsulation, and inspection.
- Collaborated with engineers to create and optimize bond programs and parameters to increase efficiency.
- Created inspection programs for X-ray machine and high magnification 3D measurement systems (VR5000).
- Used SolidWorks to design fixtures for bonding machines and machined fixtures on CNC machine.
- Designed methods for inspection and testing (both destructive and non-destructive) to validate products.
- Generate procedures and documentation for data collection to monitor process stability.

Knorr Brake Company Westminster, MD
Design Validation Intern February 2018 – August 2018, May 2019-August 2019, May 2020-August 2020*

- Utilized Creo to design Test Benches and Training Aids (A system that includes all train hardware supplied to customers, allowing operators to be trained and simulate their function through a graphical user interface).
- Designed, prototyped, and assembled pneumatic circuits.
- Collaborated with engineers to create 2D and 3D models of electrical and mechanical systems.
- Wired electrical circuits for Test Benches and Training Aids to industry standards. This includes labeling wires, following industry standards of color-coding different signal wires, and neatly organizing and grouping wires.
- Validated electrical circuits by ringing out electrical circuits to verify accuracy prior to powering the circuit.

*Internship with Knorr Brake canceled due to COVID-19 in 2020

Undergraduate Research

Modeling Settling Velocities of Nonspherical Particles in Environmental Turbulence

- Studied the motion of nonspherical and nonuniform particles through a fluid.
- Built a 3D printer to be used for printing cylinders of nonuniform density to drop into still and turbulent water.
- Utilized high speed videography to measure trajectories of falling particles and fluids surrounding them.
- Quantified settling velocity and 3D kinematics with use of 3D Particle Tracking Velocimetry.
- Conducted image processing and data processing of videography in MATLAB.

Skills

2D and 3D Modeling

- Created and managed large assemblies in order to create a bill of materials and cut sheet diagrams.
- Conducted Finite Element Analysis on heat transfer and elasticity problems in Abaqus.
- Performed computational Fluid Dynamics in SOLIDWORKS to analyze fluid flows.
- Diagramed electrical circuits in 2D CAD (BricsCAD) allowing for clear schematics for production to follow.

CNC Programming and Computational Models

- Utilized computational tools to generate toolpaths for CNC machines from 3D models.
- Performed 3D simulations on assemblies to determine maximum stress, strain, and deflections.

ADDITIONAL EXPERIENCE/HONORS

- First place in Design Showcase at Carroll County Career and Technology Center.
    - Developed an automatic garage door opening system utilizing RFID and Arduino.
- National Youth Leadership Program at University of California Berkeley (Mechanical Engineer focus).